Supporting Information for

Heterometallic Ru-Ir carbonyl clusters as catalyst precursors for hydrogenation and hydrogen transfer reactions

Francesca Forti,[a,b] Cristiana Cesari,[a,b]* Marco Bortoluzzi,[c] Cristina Femoni,[a] Maria Carmela Iapalucci,[a] and Stefano Zacchini[a,b]

[a] Dipartimento di Chimica Industriale "Toso Montanari", Università di Bologna, Viale Risorgimento 4 - 40136 Bologna. Italy.

[b] Center for Chemical Catalysis – C3, Viale Risorgimento 4 - 40136, University of Bologna, Italy.

[c] Dipartimento di Scienze Molecolari e Nanosistemi, Ca' Foscari University of Venice, Via Torino 155 – 30175 Mestre (Ve), Italy.

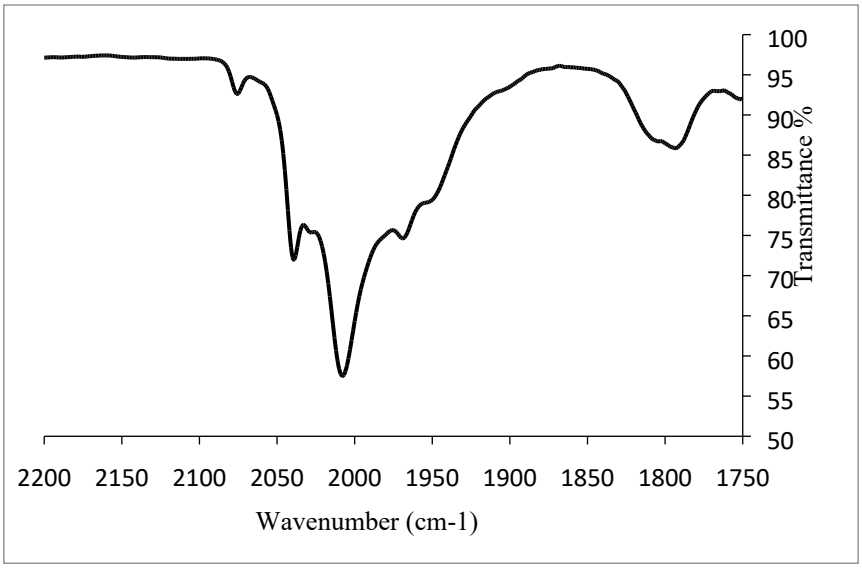

Figure S1. IR spectrum in the ν_{CO} region of $[H_2Ru_3Ir(CO)_{12}]^-$ (**2**) in CH_2Cl_2.

Figure S2. IR spectrum in the ν_{CO} region of $[HRu_3Ir(CO)_{12}]^{2-}$ (**4**) in CH_2Cl_2.

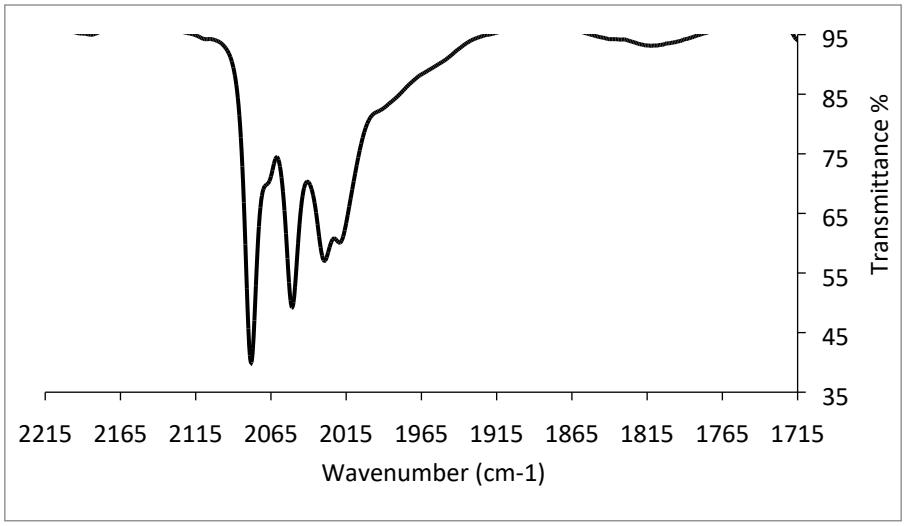

Figure S3. IR spectrum in the ν_{CO} region of $H_3Ru_3Ir(CO)_{12}$ (**3**) in CH_2Cl_2.

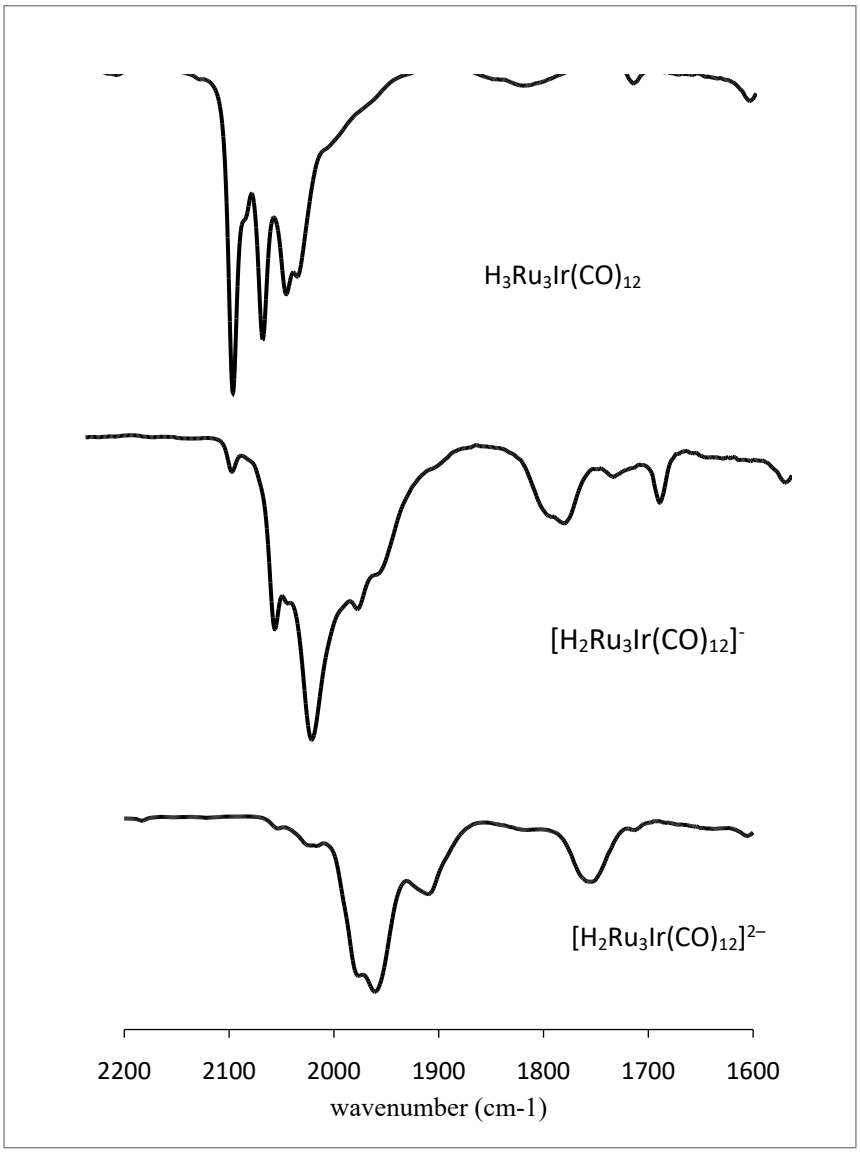

Figure S4. IR spectra in the ν_{CO} region of $[H_{3-n}Ru_3Ir(CO)_{12}]^{n-}$ (n = 0-2) in CH_2Cl_2.

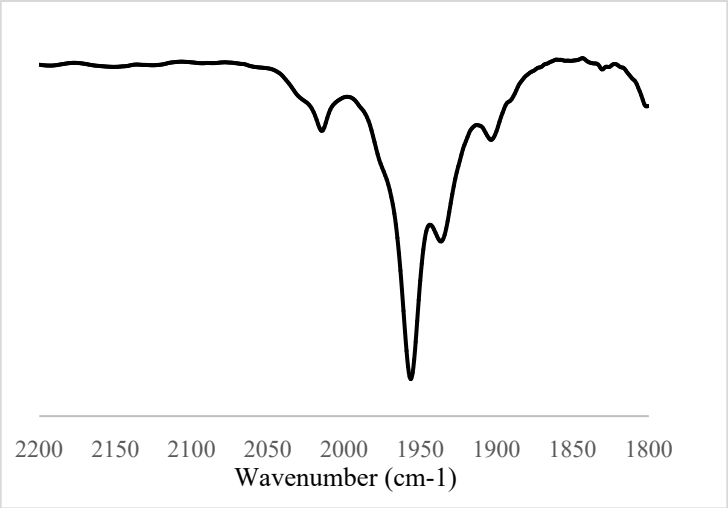

Figure S5. IR spectrum in the ν_{CO} region of $[HRu_3Rh(CO)_{12}]^{2-}$ (**6**) in acetone.

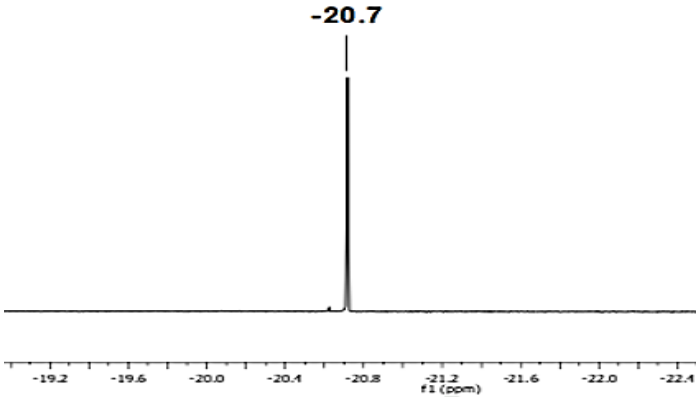

Figure S6. Hydride region of the ^{1}H NMR spectrum of $[H_2Ru_3Ir(CO)_{12}]^-$ (**2**) in CD_2Cl_2.

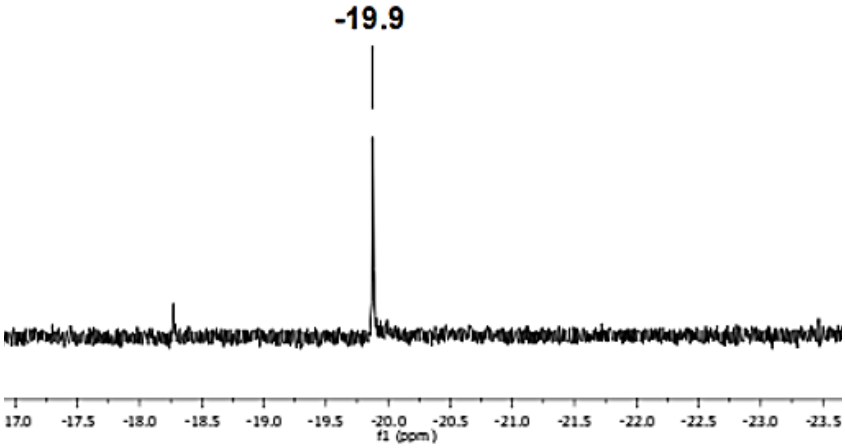

Figure S7. Hydride region of the ^{1}H NMR spectrum of $[HRu_3Ir(CO)_{12}]^{2-}$ (**4**) in CD_3COCD_3.

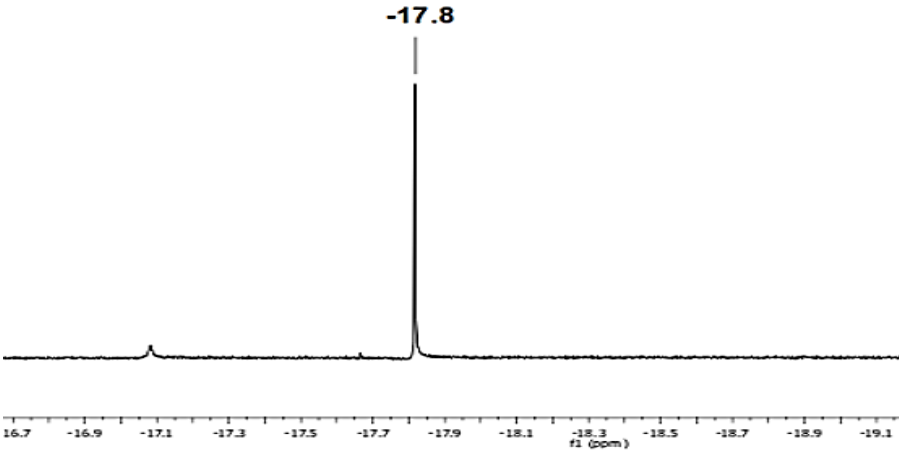

Figure S8. Hydride region of the ^{1}H NMR spectrum of $H_3Ru_3Ir(CO)_{12}$ (**3**) in CD_2Cl_2.

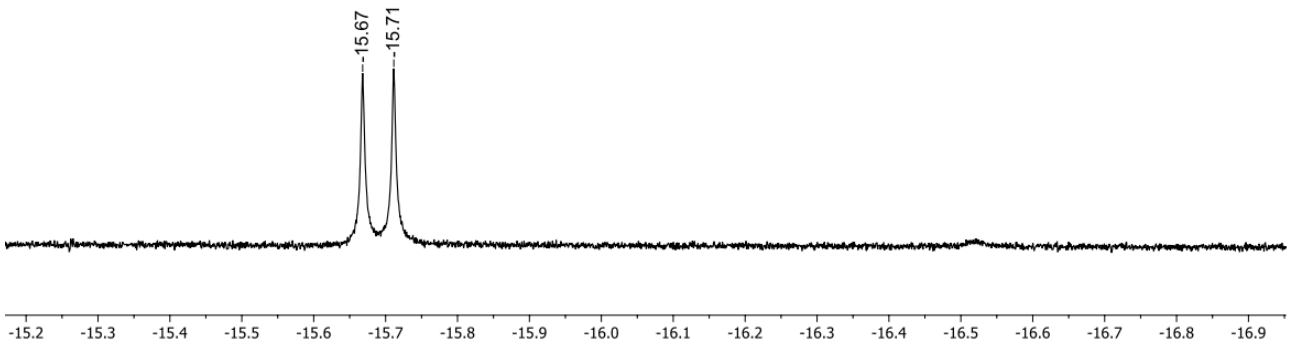

Figure S9. Hydride region of the ^{1}H NMR spectrum of $[HRu_3Rh(CO)_{12}]^{2-}$ (**6**) in acetone d_6.

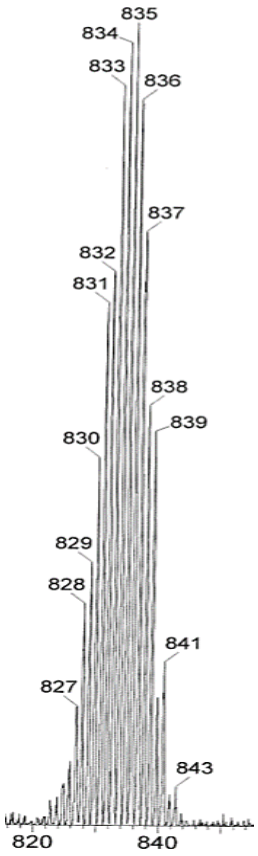

(a)

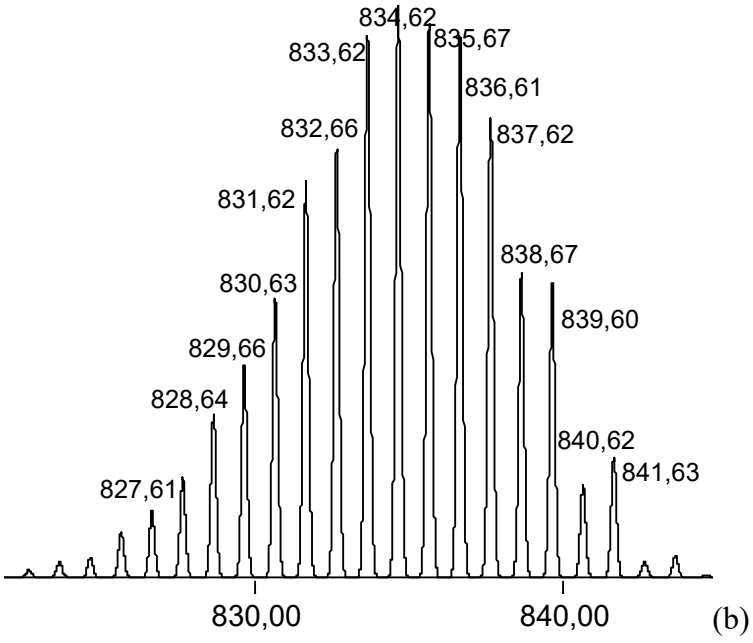

(b)

Figure S10. (a) ESI-MS spectrum in CH_3CN (ES–) of $[H_2Ru_3Ir(CO)_{12}]^-$ (**2**), and (b) simulated isotope pattern.

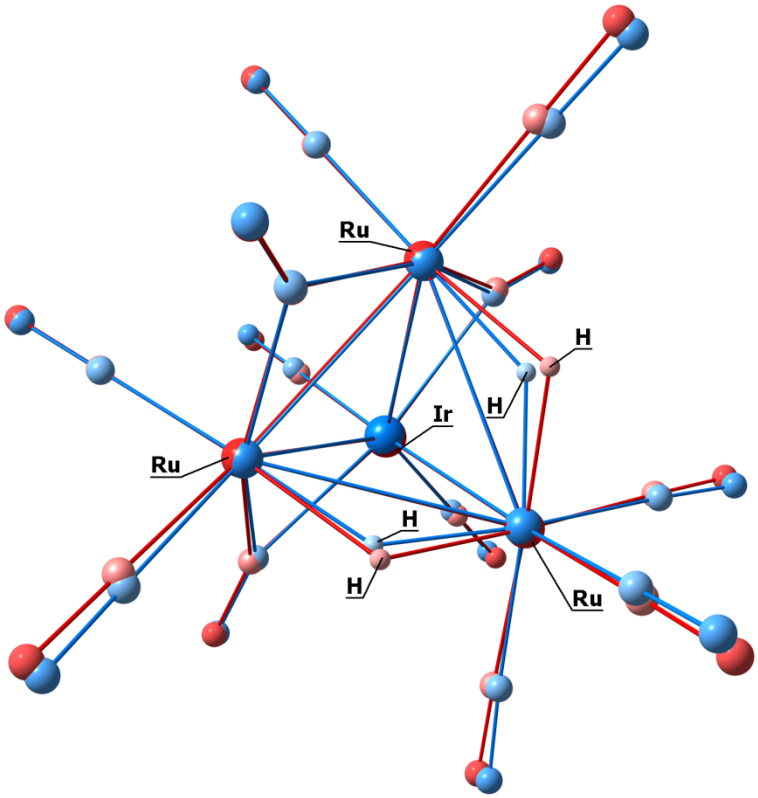

Figure S11. Best superposition of the computed (red tones) and X-ray (blue tones) structures of **2**.

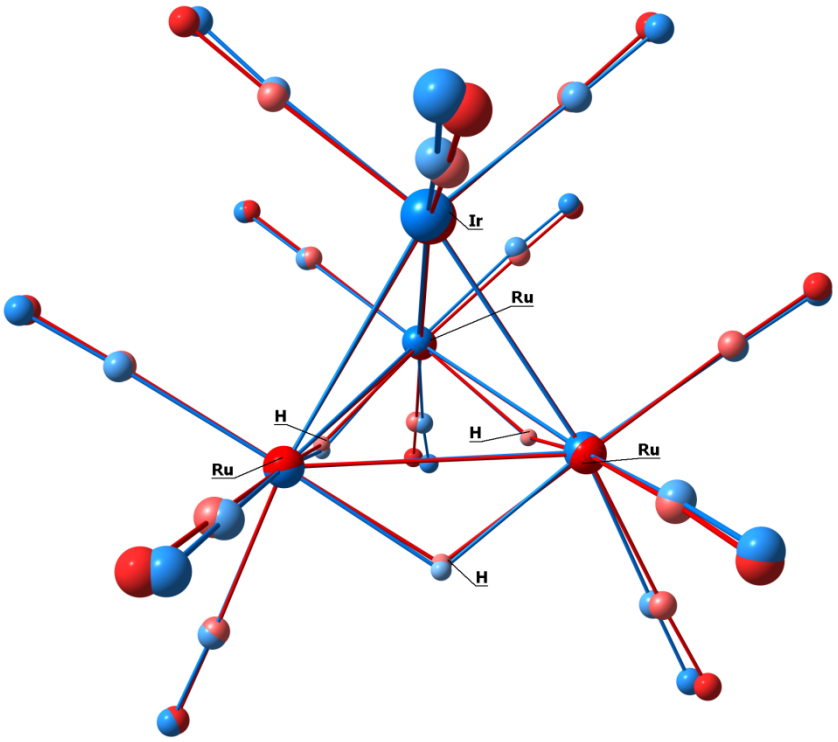

Figure S12. Best superposition of the computed (red tones) and X-ray (blue tones) structures of **3**.

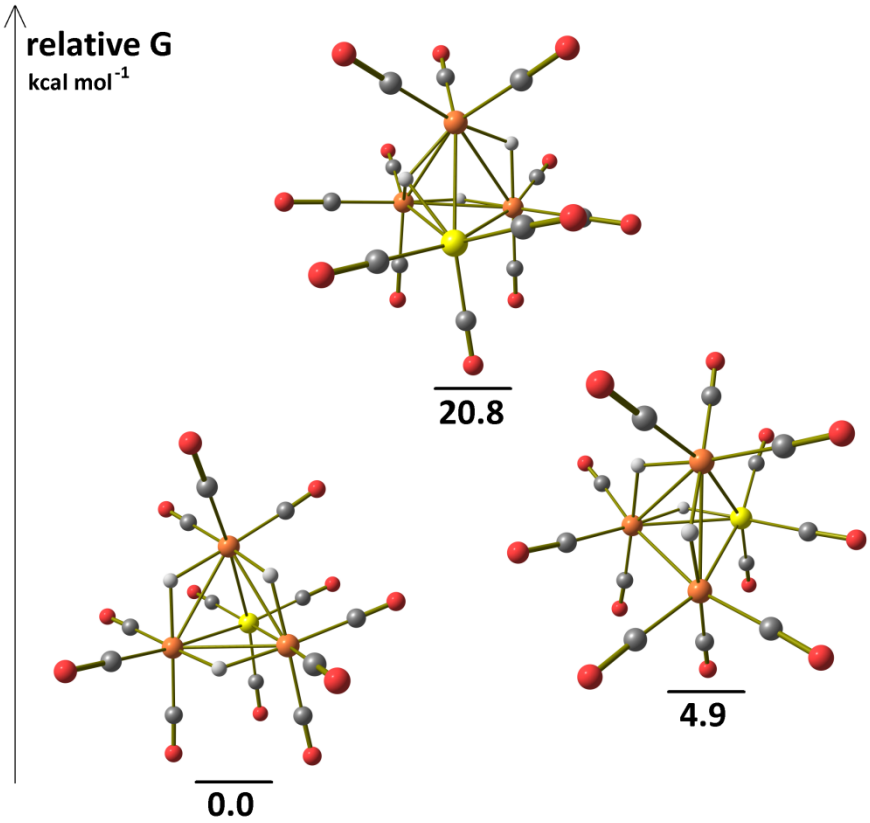

Figure S13. DFT-optimized isomers of **3** (orange Ru; yellow Ir; red O; grey C; white H) and relative Gibbs energy values (kcal mol^{-1}).

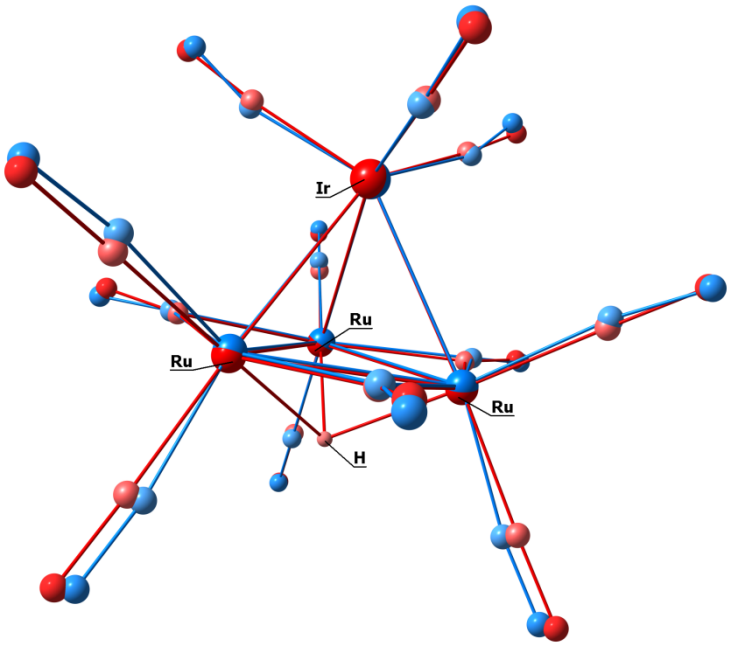

Figure S14. Best superposition of the computed (red tones) and preliminary X-ray (blue tones) structures of **4**. The hydride is present only in the computed structure.

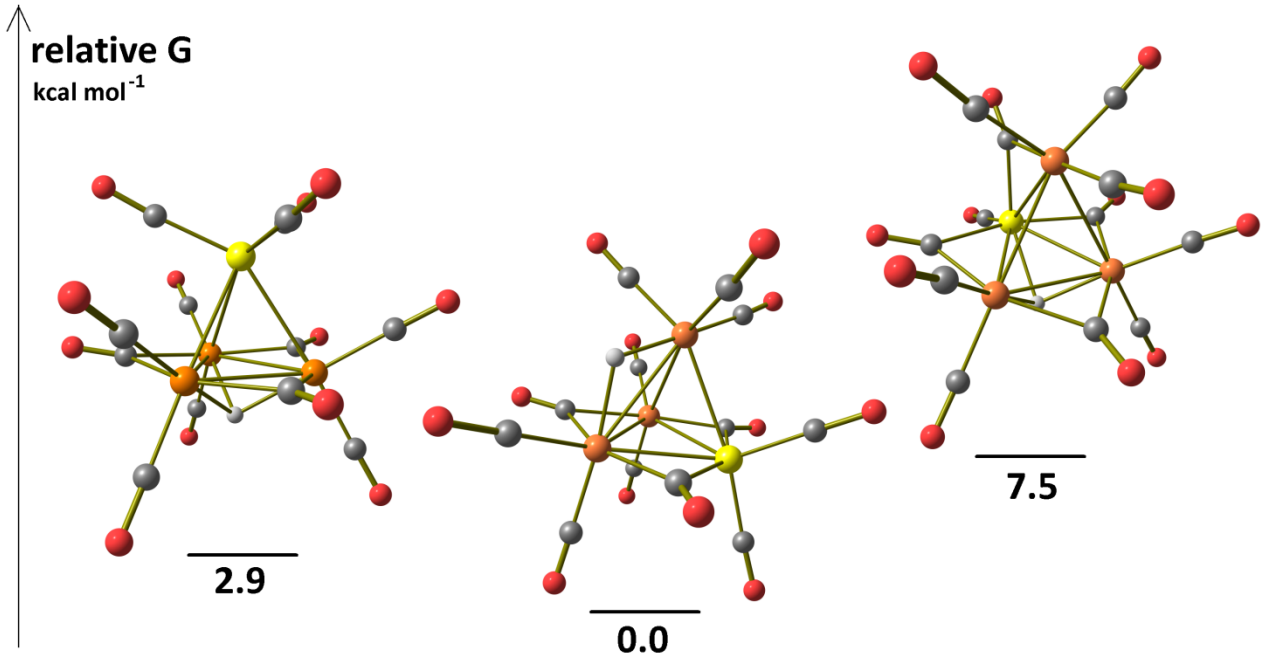

Figure S15. DFT-optimized isomers of **4** (orange Ru; yellow Ir; red O; grey C; white H) and relative Gibbs energy values (kcal mol^{-1}).

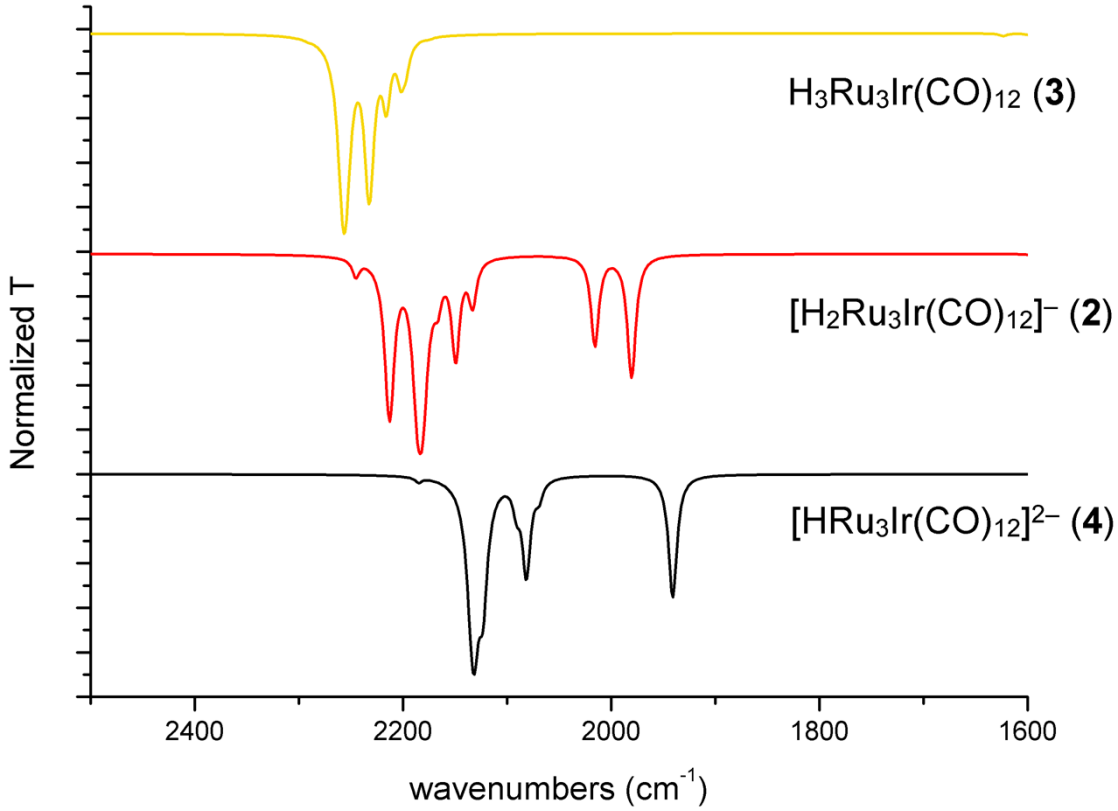

Figure S16. Unscaled simulated IR spectra of **2**, **3** and **4**. Lorentzian broadening functions, FWHM = 8 cm^{-1}.

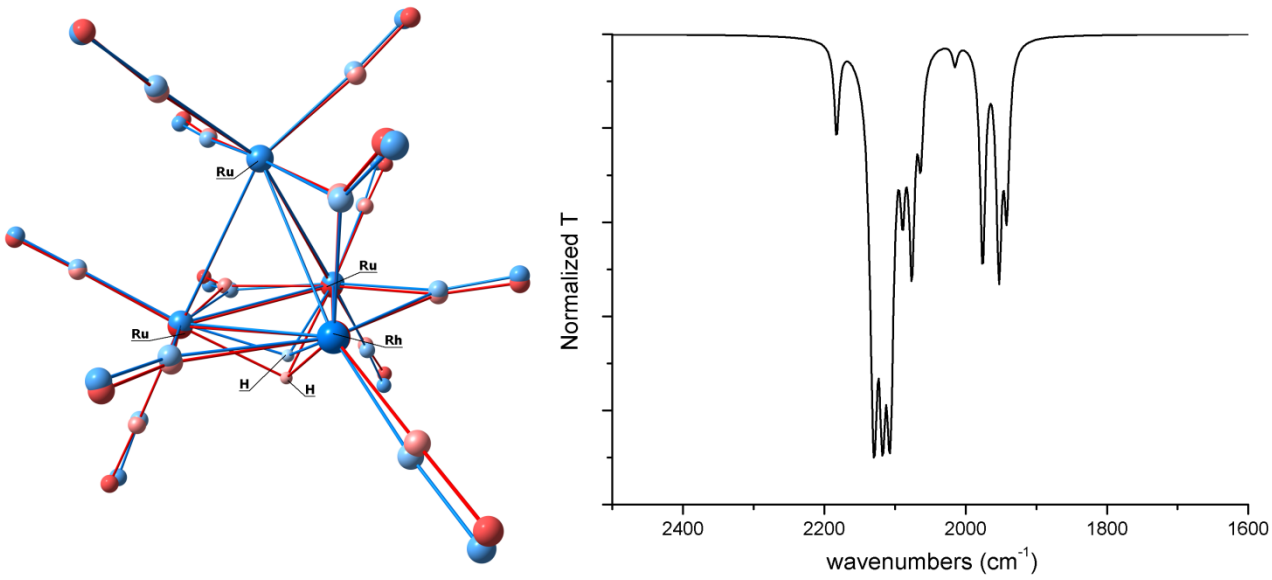

Figure S17. Best superposition of the computed (red tones) and X-ray (blue tones) structures of **6** and simulated IR spectrum (Lorentzian broadening functions, FWHM = 8 cm^{-1}).

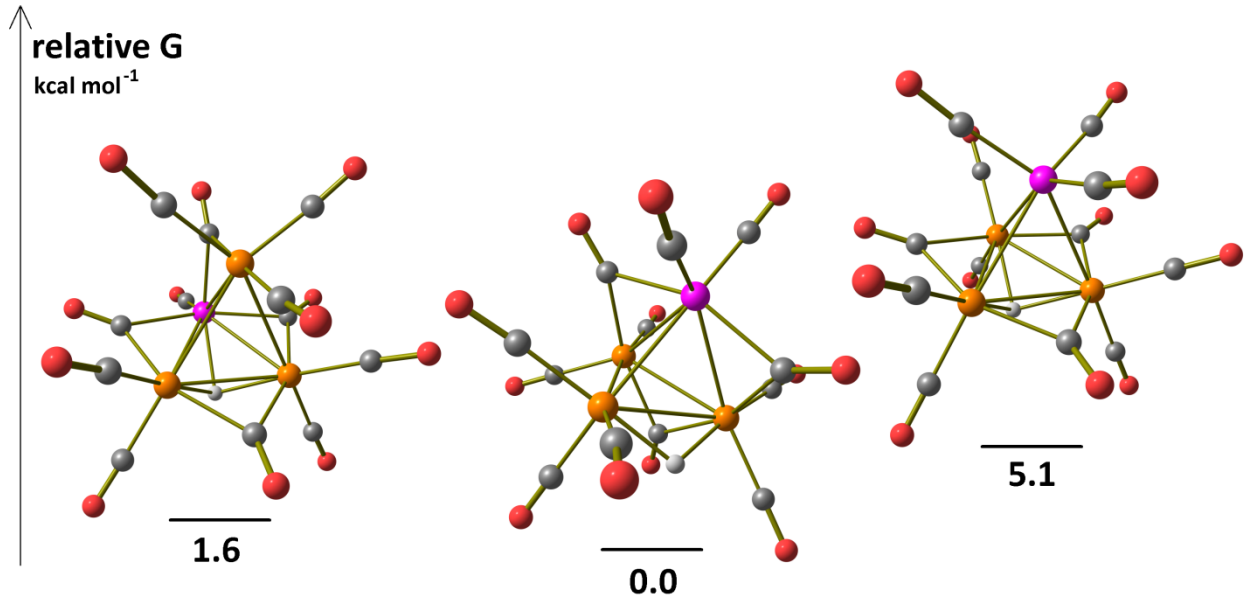

Figure S18. DFT-optimized isomers of **6** (orange Ru; purple Rh; red O; grey C; white H) and relative Gibbs energy values (kcal mol^{-1}).

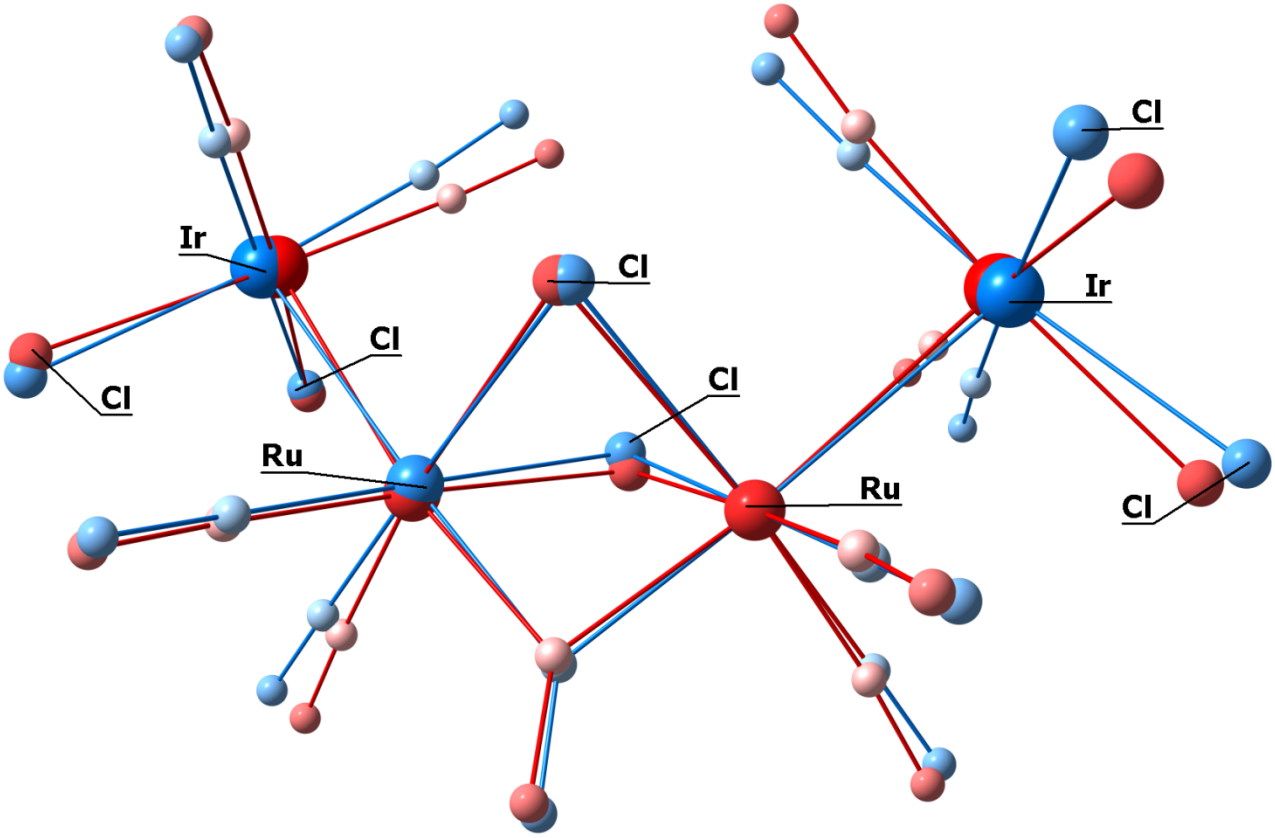

Figure S19. Best superposition of the computed (red tones) and X-ray (blue tones) structures of **5**.

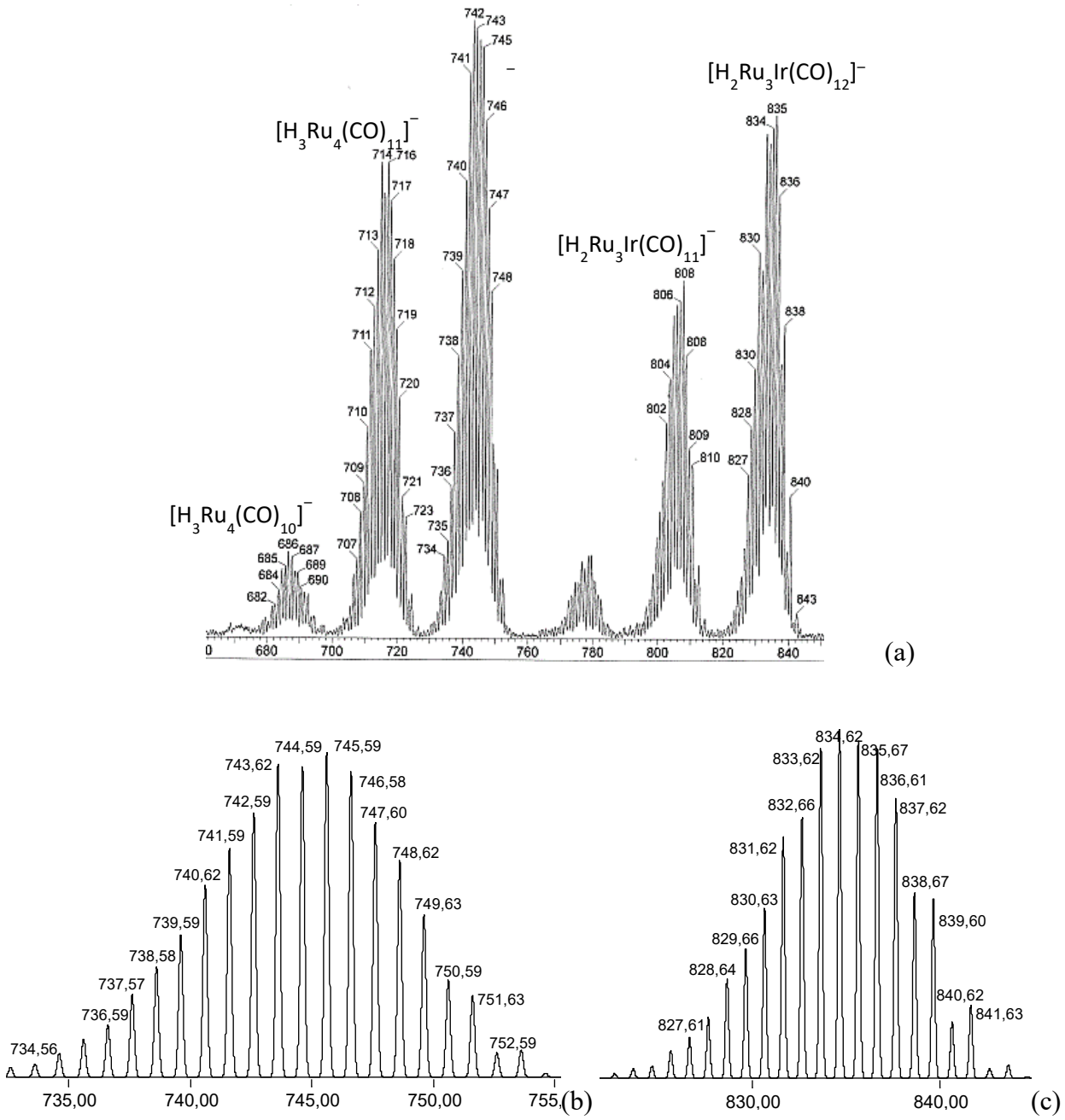

Figure S20. (a) ESI-MS spectrum in CH_3OH (ES–) of the mixture at the end of the reactivity experiment: $[NEt_4][H_2Ru_3Ir(CO)_{12}]$ ($[NEt_4][$**2**$]$) in ^{i}PrOH, for 24 h at 82 °C. Simulated isotope patterns of (b) $[H_3Ru_4(CO)_{12}]^-$, and (c) $[H_2Ru_3Ir(CO)_{12}]^-$.

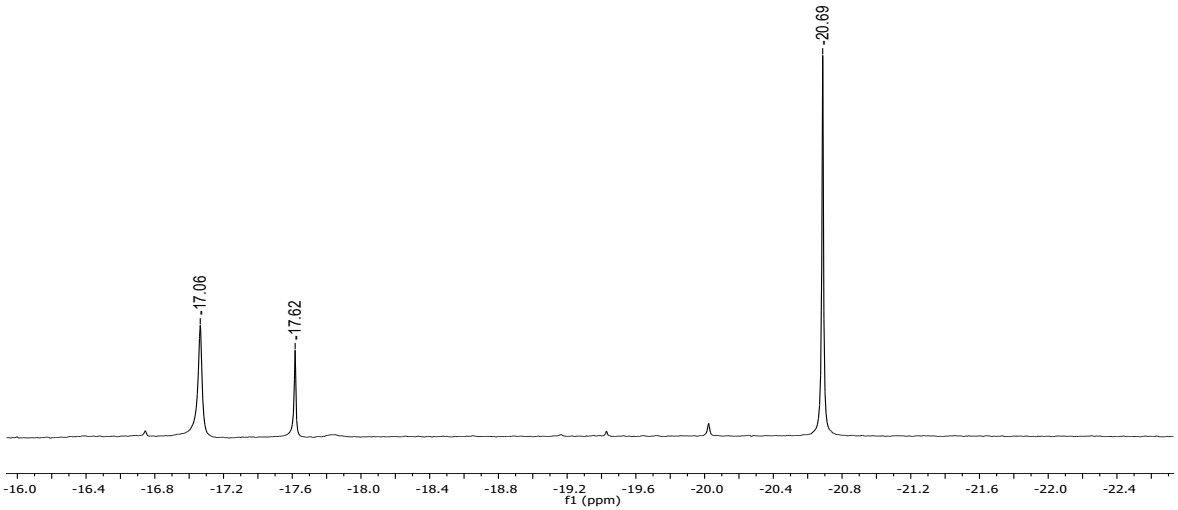

Figure S21. ^{1}H NMR spectrum in CD_2Cl_2 of the mixture at the end of the reactivity experiment: $[NEt_4][H_2Ru_3Ir(CO)_{12}]$ ($[NEt_4][$**2**$]$) in ^{i}PrOH, for 24 h at 82 °C.

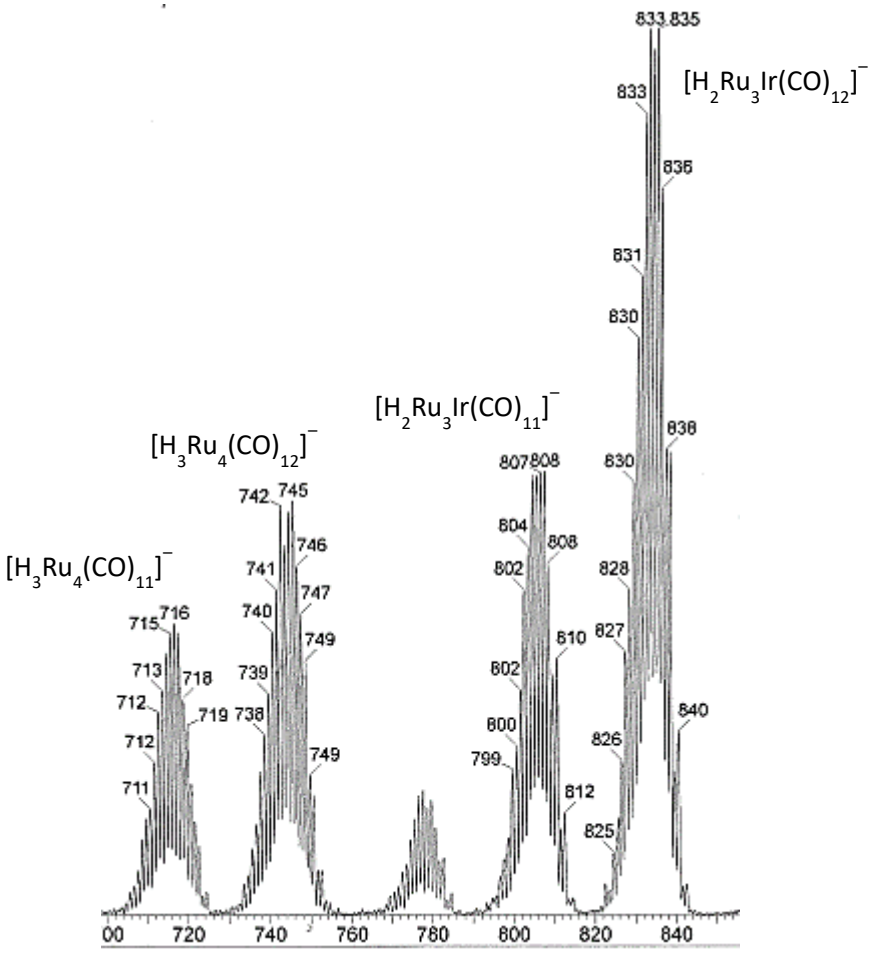

Figure S22. ESI-MS spectrum in CH_3OH (ES–) of the mixture at the end of the reactivity experiment: $[NEt_4][H_2Ru_3Ir(CO)_{12}]$ ($[NEt_4][$**2**$]$) in ^{i}PrOH, for 24 h at 82 °C, in the presence of substrate 4-Fluoroacetophenone (1 eq).

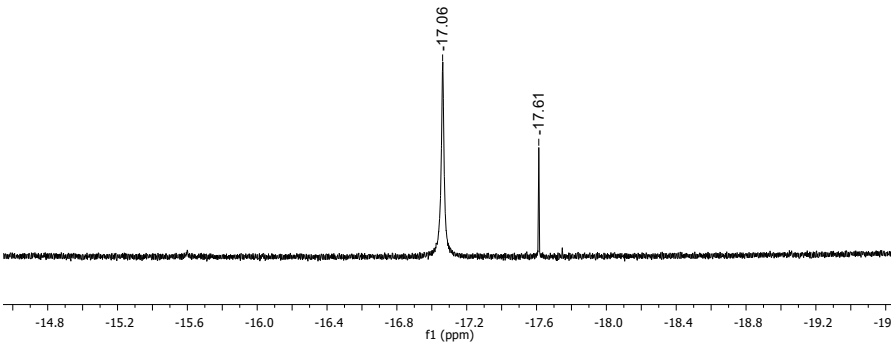

Figure S23. ^{1}H NMR spectrum in CD_2Cl_2 of the mixture at the end of the reactivity experiment: $[NEt_4][H_2Ru_3Ir(CO)_{12}]$ ($[NEt_4][$**2**$]$) in ^{i}PrOH, for 24 h at 82 °C, in the presence of substrate 4-Fluoroacetophenone (1 eq).

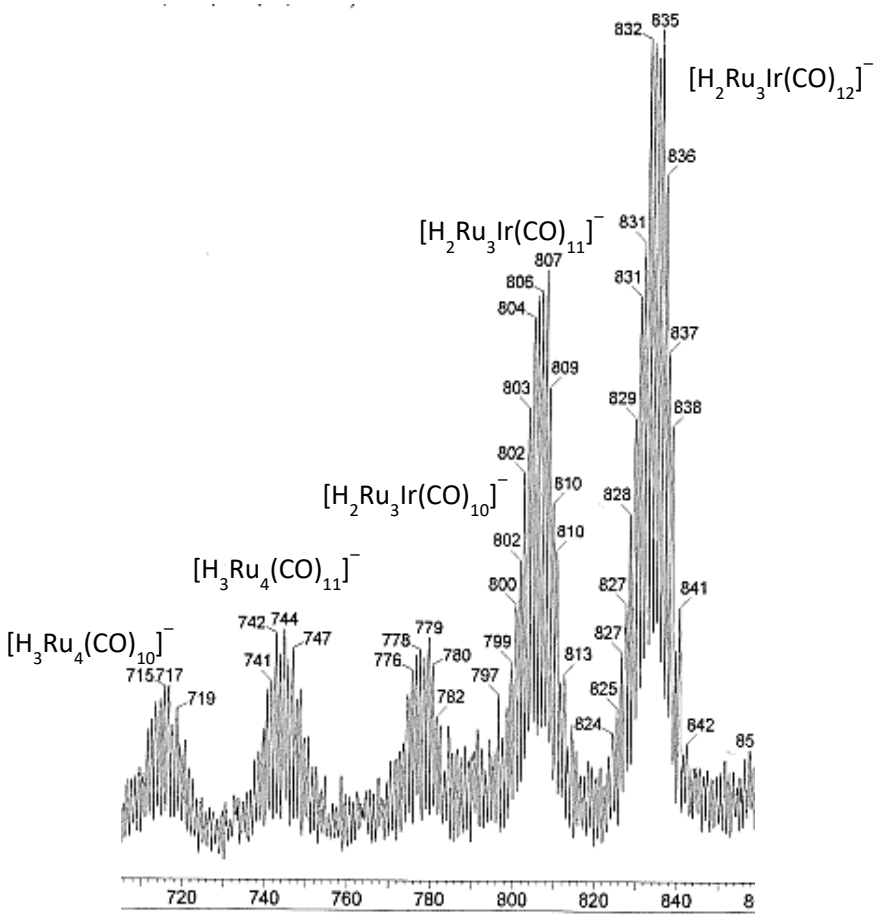

Figure S24. ESI-MS spectrum in CH_3OH (ES–) of the mixture at the end of the reactivity experiment: $[NEt_4][H_2Ru_3Ir(CO)_{12}]$ ($[NEt_4][$**2**$]$) in ^{i}PrOH, for 24 h at 82 °C, in the presence of substrate 4-Fluoroacetophenone (1 eq) and base KO^{t}Bu (10 eq).

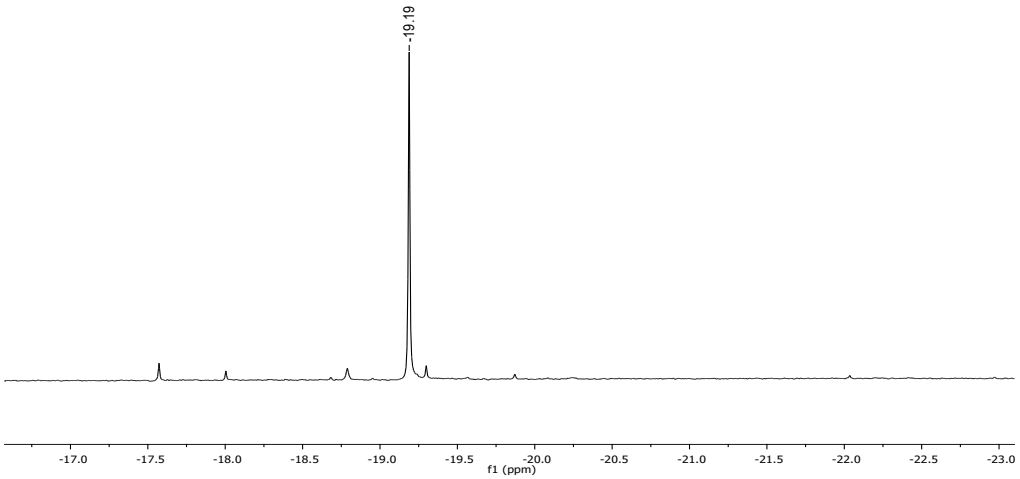

Figure S25. ^{1}H NMR spectrum in $(CD_3)_2CO$ of the mixture at the end of the reactivity experiment: $[NEt_4][H_2Ru_3Ir(CO)_{12}]$ ($[NEt_4][$**2**$]$) in ^{i}PrOH, for 24 h at 82 °C, in the presence of substrate 4-Fluoroacetophenone (1 eq) and base KO^{t}Bu (10 eq).

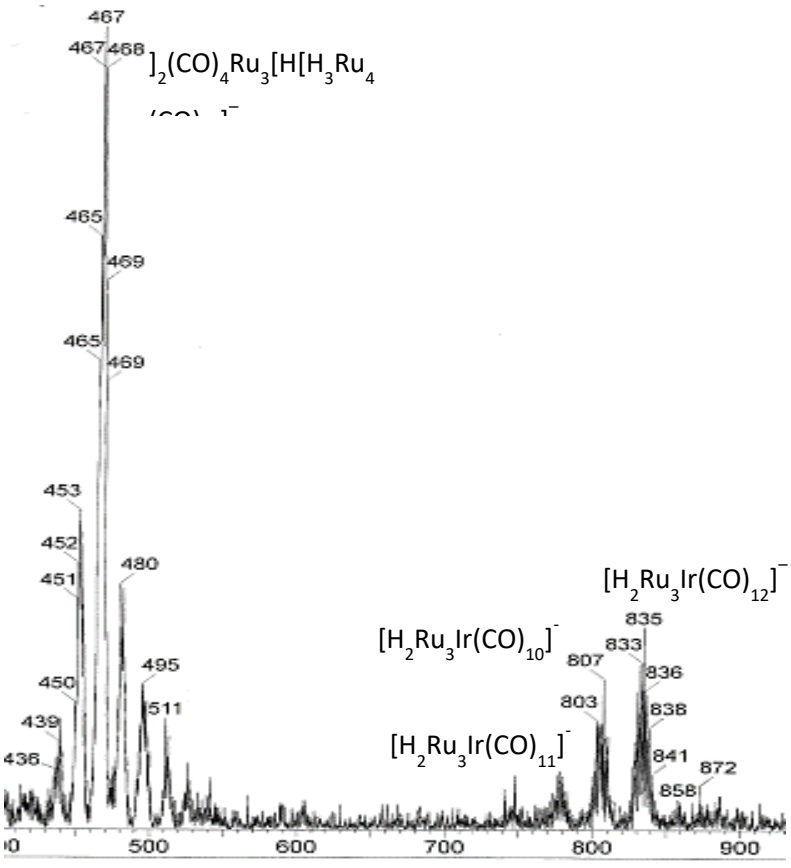

Figure S26. ESI-MS spectrum in CD_3CN (ES–) of the mixture at the end of the reactivity experiment: $[NEt_4]_2[HRu_3Ir(CO)_{12}]$ ($[NEt_4]_2[$**4**$]$) in ^{i}PrOH, for 24 h at 82 °C, in the presence of base KO^{t}Bu (10 eq).

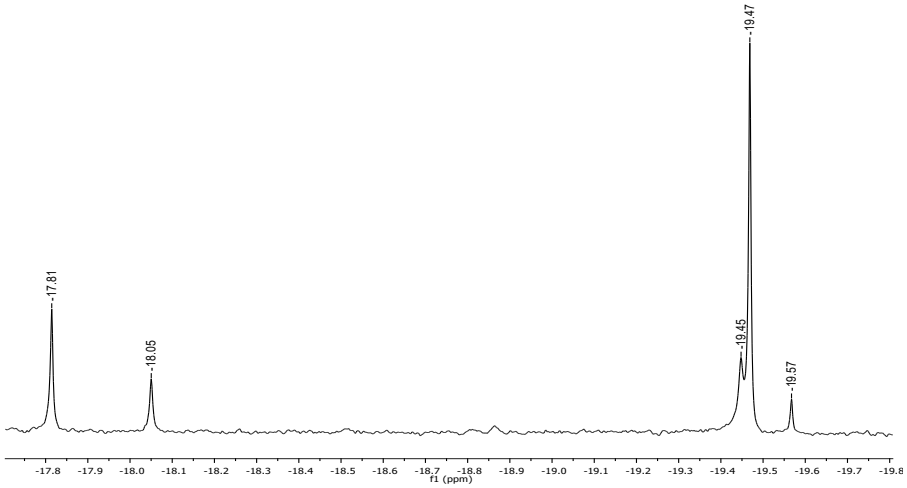

Figure S27. ^{1}H NMR spectrum in CD_3CN of the mixture at the end of the reactivity experiment: $[NEt_4]_2[HRu_3Ir(CO)_{12}]$ ($[NEt_4]_2$[**4**]) in ^{i}PrOH, for 24 h at 82 °C, in the presence of base KO^{t}Bu (10 eq).

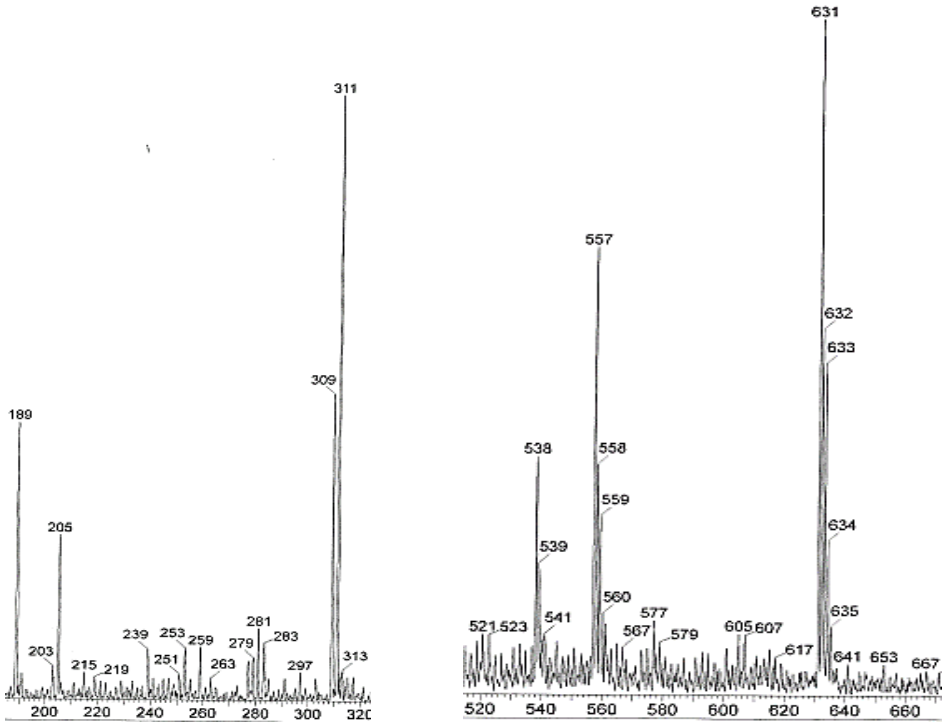

Figure S28. ESI-MS spectrum in CD_3CN (ES–) of the mixture at the end of the reactivity experiment: $H_3Ru_3Ir(CO)_{12}$ (**3**) in ^{i}PrOH, for 24 h at 82 °C, in the presence of base KO^{t}Bu (10 eq).

Table S1. Catalytic transfer hydrogenation of 4-fluoroacetophenone with heterometallic - Control Experiments.

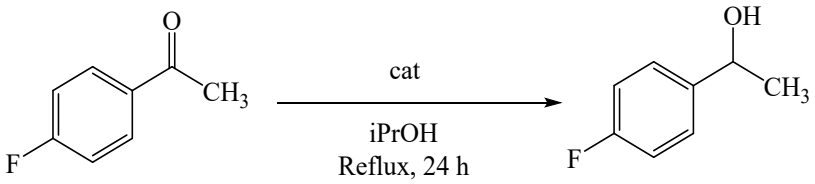

Entry	cat	cat (mol %)	KO^{t}Bu (mol %)	Conversion (%) 5 h	Conversion (%) 24 h
1-blank	none	/	/	n.d.	n.d.
2-blank		/	10	n.d.	n.d.
1-Ru	$RuCl_3 \cdot 3H_2O$	1	/	n.d.	n.d.
1-Ir	$IrCl_3 \cdot 3H_2O$	1	/	n.d.	n.d.
2-Ir	$[Ir(COD)Cl]_2$	1	/	n.d.	n.d.

General conditions: catalyst (3 µmol, 1% mol/mol), ^{i}PrOH (5 mL), KO^{t}Bu (10 mol% when added), 4-Fluoroacetophenone (36.5 µL, 300 µmol), T = 82°C, N_2 atmosphere; the conversions were determined by ^{19}F NMR spectroscopy.

Table S2. Catalytic transfer hydrogenation of 4-fluoroacetophenone with heterometallic $[NEt_4]$[**2**] with longer reaction time.

cat	cat (mol %)	KO^{t}Bu (mol %)	Conversion (%) 24 h	Conversion (%) 30 h	Conversion (%) 48 h	Conversion (%) 54 h	Conversion (%) 72 h	Conversion (%) 78 h
$[NEt_4]$[**2**]	1	10	85	86	90	>95	100	100

General conditions: catalyst (3 µmol, 1% mol/mol), ^{i}PrOH (5 mL), KO^{t}Bu (10 mol %), and 4-fluoroacetophenone (36.5 µL, 300 µmol), T = 82 °C, N_2 atmosphere; the conversions were determined by ^{19}F-NMR spectroscopy. All entries are the average of at least three independent catalytic runs.

Table S3. Catalytic transfer hydrogenation of 4-fluoroacetophenone with heterometallic $[NEt_4][\mathbf{2}]$ in presence of metallic mercury.

Entry	cat	cat (mol %)	KO^tBu (mol %)	Conversion (%) 1h	Conversion (%) 3h	Conversion (%) 5h	Conversion (%) 24h
1-2	$[NEt_4][\mathbf{2}]$	1	/	0	27	48	59
2-2		1	10	0	0	<5	42

General conditions: catalyst (3 μmol, 1 mol %), ^{i}PrOH (5 mL), KO^tBu (10 mol % when needed), and 4-fluoroacetophenone (36.5 μL, 300 μmol), T = 82 °C, a small amount of metallic mercury, N_2 atmosphere; the conversions were determined by ^{19}F NMR spectroscopy. All entries are the average of at least three independent catalytic runs.

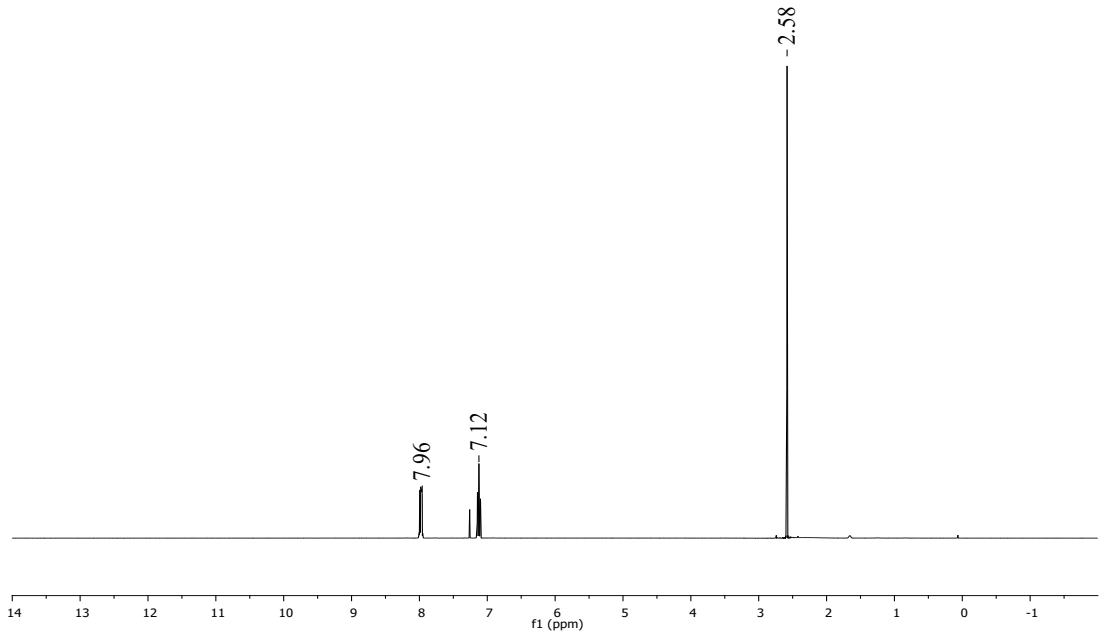

Figure S29. ^{1}H NMR spectrum of the reagent 4-fluoroacetophenone in $CDCl_3$.

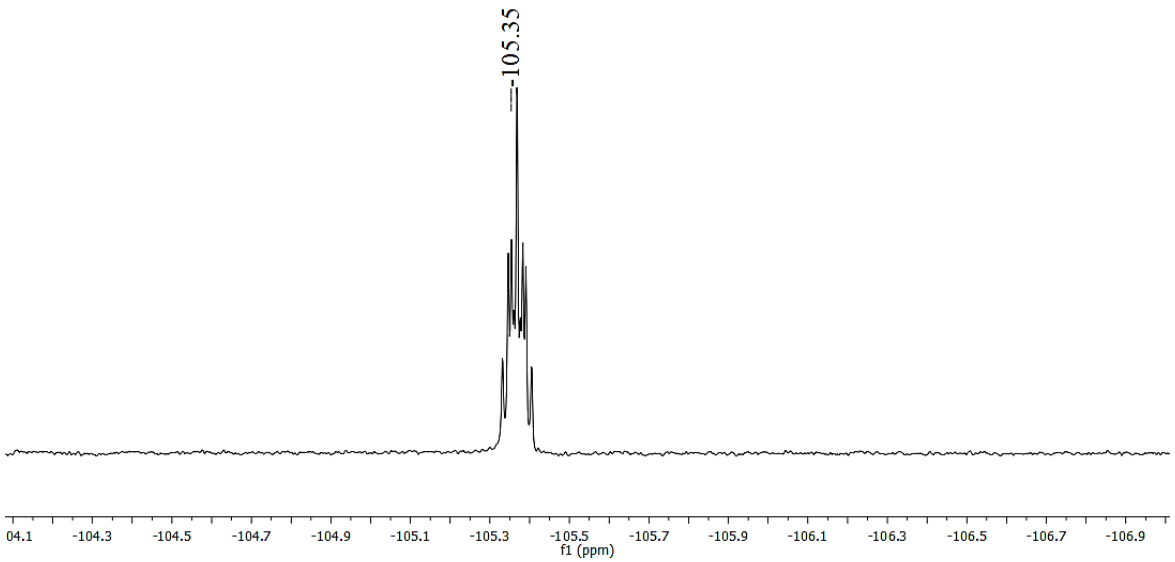

Figure S30. ^{19}F NMR spectrum of the reagent 4-fluoroacetophenone in $CDCl_3$.

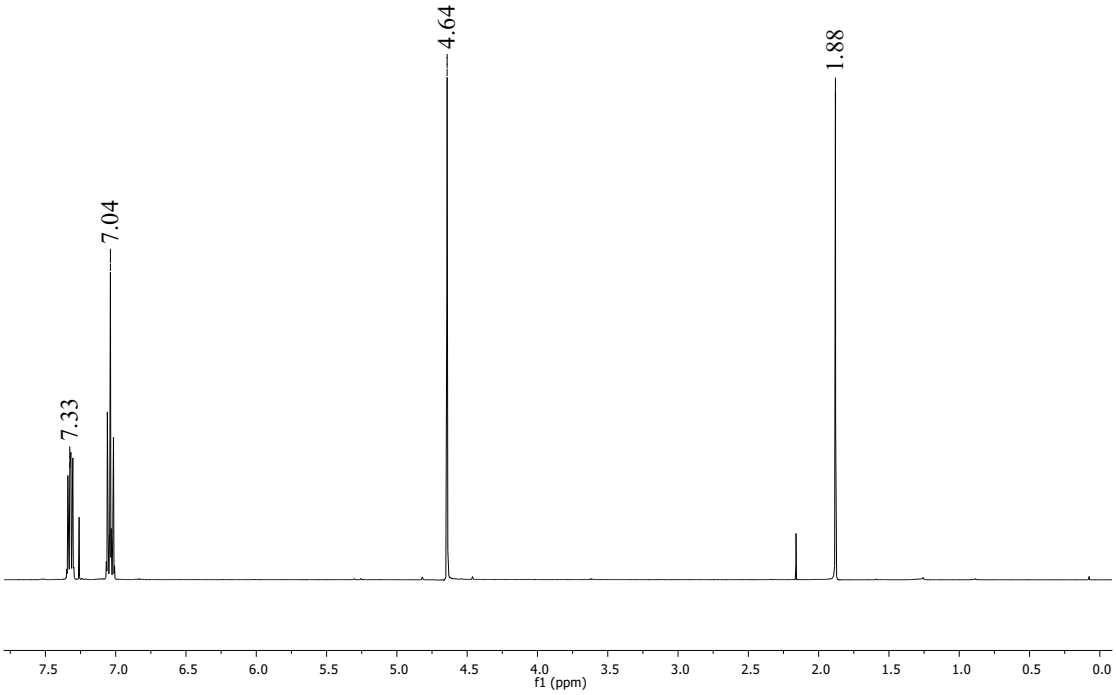

Figure S31. ^{1}H NMR spectrum of the product [1-(4-fluorophenyl)ethan-1-ol] in $CDCl_3$.

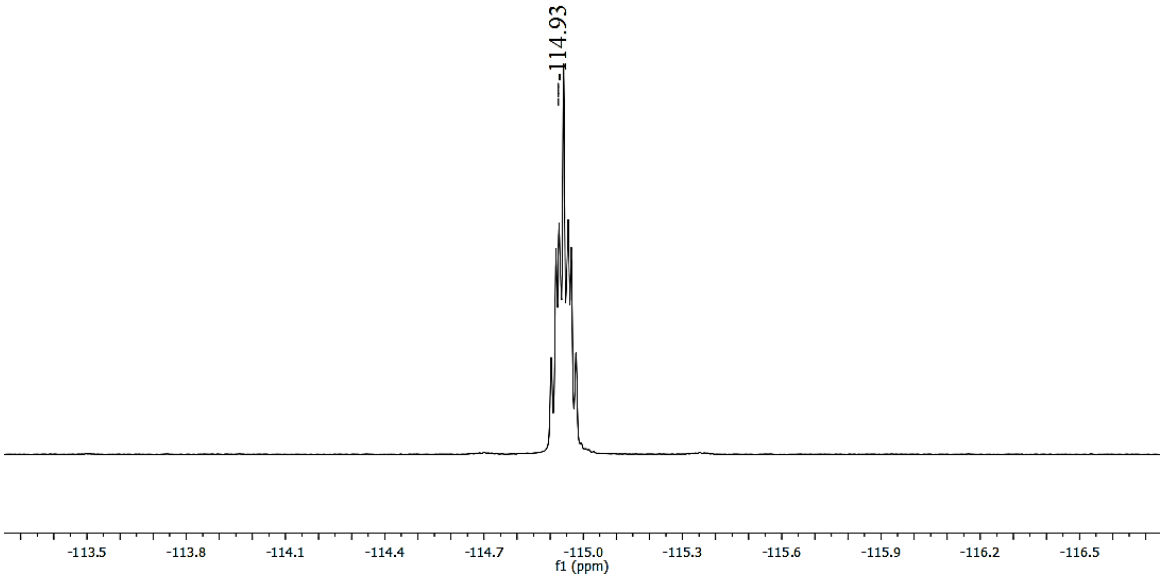

Figure S32. ^{19}F NMR spectrum of the product [1-(4-fluorophenyl)ethan-1-ol] in $CDCl_3$.

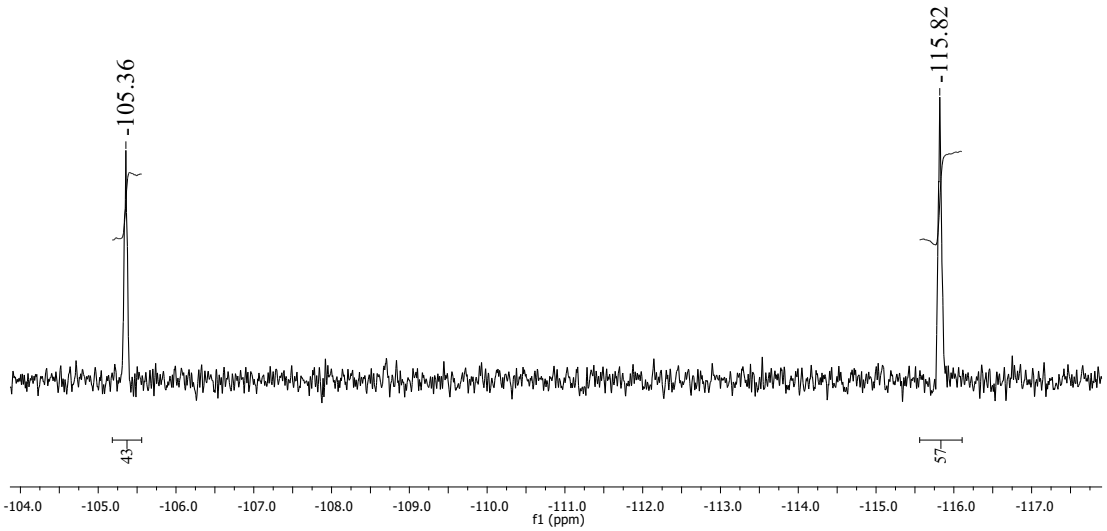

Figure S33. ^{19}F NMR spectrum of a typical reaction mixture at the end of catalytic transfer hydrogenation of 4-fluoroacetophenone in $CDCl_3$.

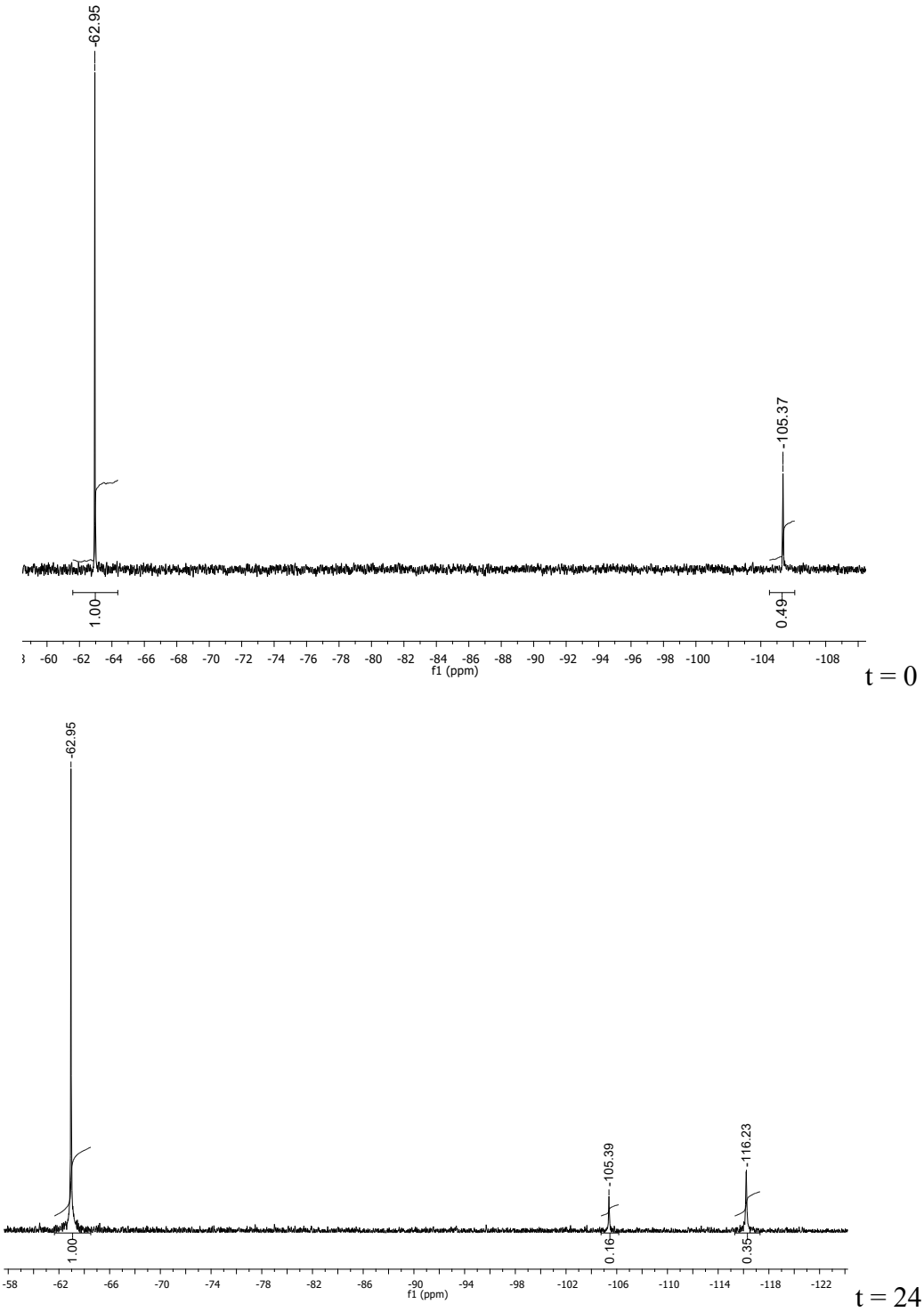

Figure S34. ^{19}F NMR spectra at the begin and at the end of catalytic transfer hydrogenation of 4-fluoroacetophenone in $CDCl_3$ in the presence of the internal standard α,α,α-trifluorotoluene.

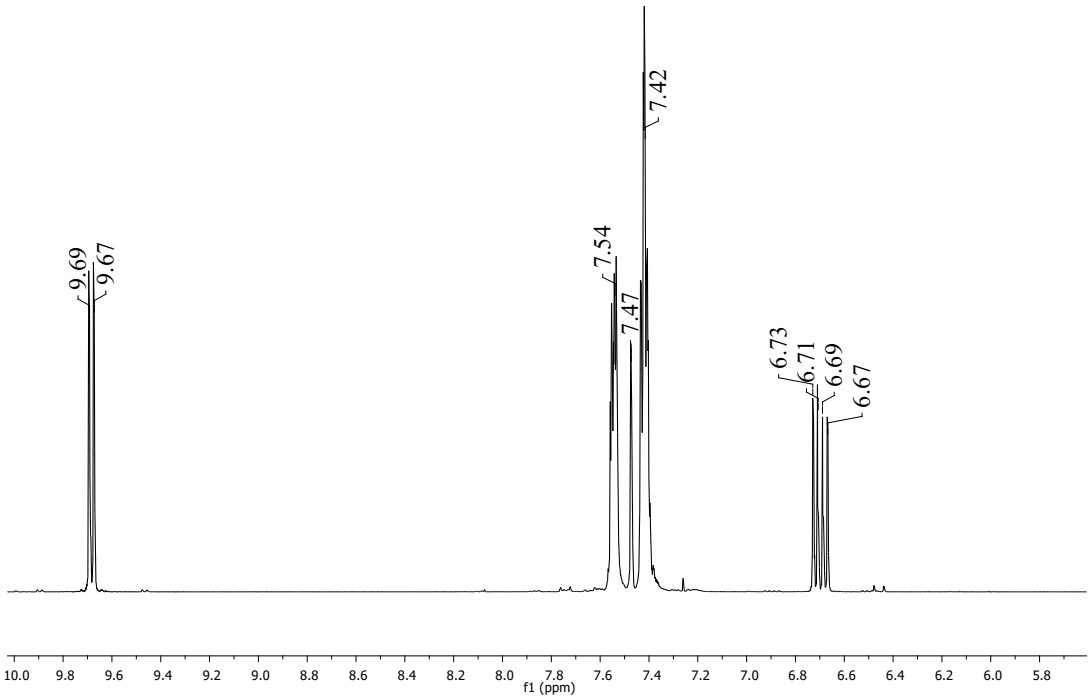

Figure S35. ^{1}H NMR spectrum of the reagent trans-cinnamaldehyde in $CDCl_3$.

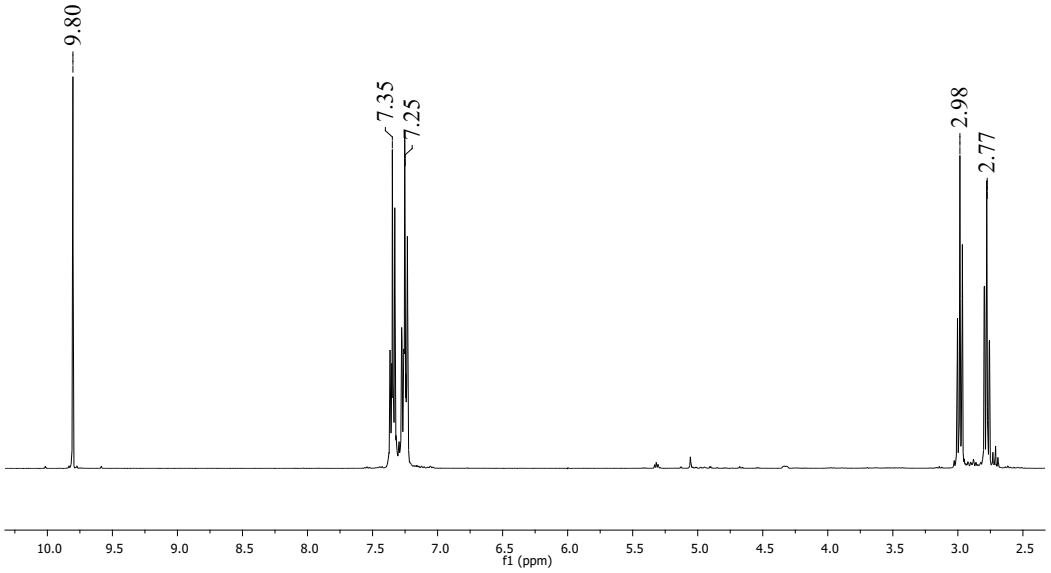

Figure S36. ^{1}H NMR spectrum of the product 3-phenylpropionaldehyde in $CDCl_3$.

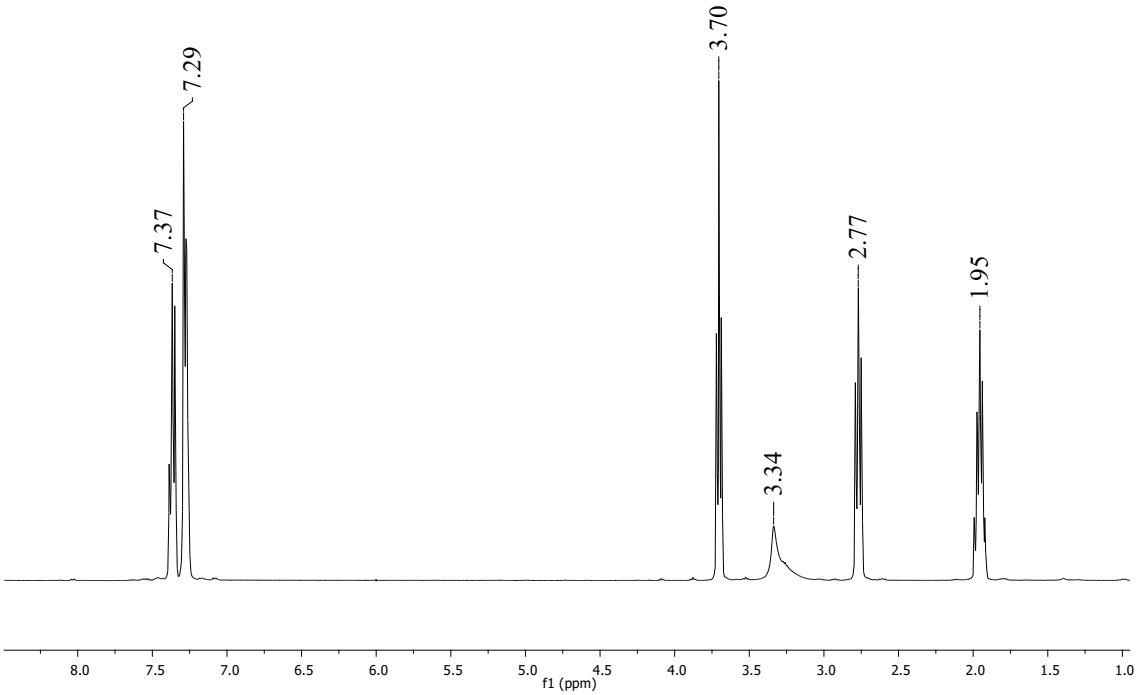

Figure S37. ^{1}H NMR spectrum of the product 3-phenyl-1-propanol in $CDCl_3$.

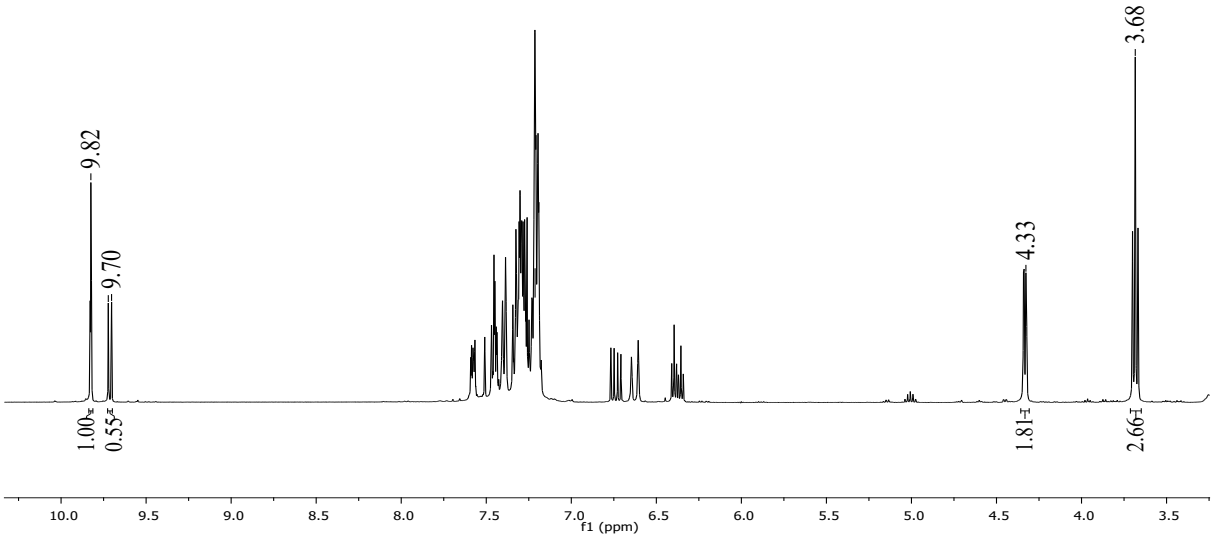

Figure S38. ^{1}H NMR spectrum of a typical reaction mixture at the end of catalytic hydrogenation of trans-cinnamaldehyde in $CDCl_3$; integrals of resonance of reagent and products, which have been used to calculate yield and selectivity, have been shown in the picture. From left to right: 3-phenylpropionaldehyde (**a**, 1H), trans-cinnamaldehyde (**s**, 1H), cinnamyl alcohol (**b**, 2H), 3-phenyl-1-propanol (**c**, 2H).

Example of the calculation of conversion of 3-phenyl-1-propanol (**c**) used to obtain selectivity and yield values at the end of catalytic hydrogenation of trans-cinnamaldehyde (one characteristic peak for every compound has been used, as described in Figure S37):

$$\frac{\frac{\int c}{2}}{\int s + \int a + \frac{\int b}{2} + \frac{\int c}{2}}$$

Table S4. Crystal data and experimental details for $[NEt_4][H_2Ru_3Ir(CO)_{12}]$ ($[NEt_4][$**2**$]$), $H_3Ru_3Ir(CO)_{12}$ (**3**), $[NEt_4]_2[Ru_3Ir_2Cl_6(CO)_9]$ ($[NEt_4]_2[$**5**$]$), and $[NEt_4]_2[HRu_3Rh(CO)_{12}]$ ($[NEt_4]_2[$**6**$]$).

	$[NEt_4][H_2Ru_3Ir(CO)_{12}]$	**$H_3Ru_3Ir(CO)_{12}$**
Formula	$C_{20}H_{22}IrNO_{12}Ru_3$	$C_{12}H_3IrO_{12}Ru_3$
Fw	963.79	834.55
T, K	100(2)	100(2)
λ, Å	0.71073	0.71073
Crystal system	Orthorhombic	Triclinic
Space Group	*Pbcm*	$P\bar{1}$
a, Å	12.4677(17)	8.2134(5)
b, Å	12.4103(17)	9.0794(6)
c, Å	17.630(3)	13.5190(8)
α, °	90	82.711(2)
β, °	90	80.357(2)
γ, °	90	68.689(2)
Cell Volume, $Å^3$	2727.9(7)	923.55(10)
Z	4	2
D_c, g cm^{-3}	2.347	3.001
μ, mm^{-1}	6.551	9.648
F(000)	1816	760
Crystal size, mm	0.16×0.13×0.11	0.16×0.13×0.10
θ limits, °	1.633-25.098	2.414-25.097
Index ranges	$-14 \le h \le 14$ $-14 \le k \le 14$ $-21 \le l \le 21$	$-9 \le h \le 9$ $-10 \le k \le 10$ $-16 \le l \le 16$
Reflections collected	44897	14898
Independent reflections	2517 [R_{int} = 0.1677]	3295 [R_{int} = 0.0803]
Completeness to θ max	100.0%	99.9%
Data / restraints / parameters	2517 / 68 / 187	3295 / 16 / 262
Goodness on fit on F^2	1.086	1.086
R_1 ($I > 2\sigma(I)$)	0.0597	0.0341
wR_2 (all data)	0.1673	0.0920
Largest diff. peak and hole, e $Å^{-3}$	3.561 / -1.585	3.846 / -2.423

	$[NEt_4]_2[Ru_3Ir_2Cl_6(CO)_9]$	**$[NEt_4]_2[HRu_3Rh(CO)_{12}]$**
Formula	$C_{25}H_{40}Cl_6Ir_2N_2O_9Ru_2$	$C_{28}H_{41}N_2O_{12}RhRu_3$
Fw	1311.83	1003.75
T, K	100(2)	100(2)
λ, Å	0.71073	0.71073
Crystal system	Monoclinic	Monoclinic
Space Group	$P2_1/n$	$P2_1/n$
a, Å	15.1802(11)	11.966(2)
b, Å	17.3645(13)	19.837(4)
c, Å	15.3305(12)	15.038(3)
α, °	90	90
β, °	104.418(2)	91.344(7)
γ, °	90	90
Cell Volume, $Å^3$	3913.8(5)	3568.3(11)
Z	4	4
D_c, g cm^{-3}	2.226	1.868
μ, mm^{-1}	7.991	1.758
F(000)	2480	1984
Crystal size, mm	0.15×0.12×0.10	0.15×0.12×0.07
θ limits, °	1.689–26.000	1.700–25.027
Index ranges	$-18 \le h \le 18$ $-21 \le k \le 21$ $-18 \le l \le 18$	$-14 \le h \le 14$ $-23 \le k \le 23$ $-17 \le l \le 17$
Reflections collected	52136	35606
Independent reflections	7692 [R_{int} = 0.0353]	6296 [R_{int} = 0.11547]
Completeness to θ max	100.0%	100.0%
Data / restraints / parameters	7692 / 227 / 492	6296 / 815 / 544
Goodness on fit on F^2	1.237	1.124
R_1 ($I > 2\sigma(I)$)	0.0295	0.1240
wR_2 (all data)	0.0588	0.3194
Largest diff. peak and hole, e $Å^{-3}$	2.192 / –0.925	7.205 / –2.345

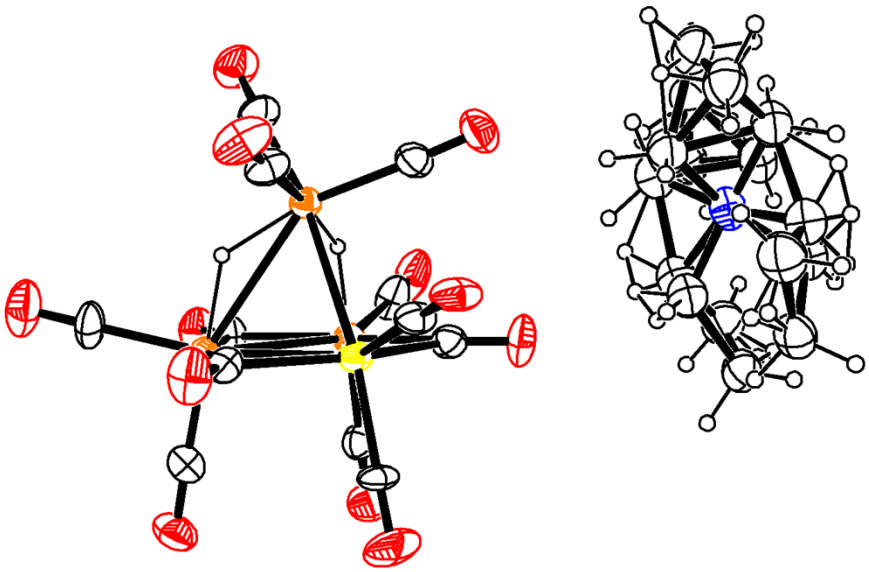

Figure S39. ORTEP drawing of $[NEt_4][H_2Ru_3Ir(CO)_{12}]$ ($[NEt_4][$**2**$]$) (orange Ru; yellow Ir; red O; blue N; grey C; white H). Thermal ellipsoids are at the 30% probability level. Disordered atoms are included.

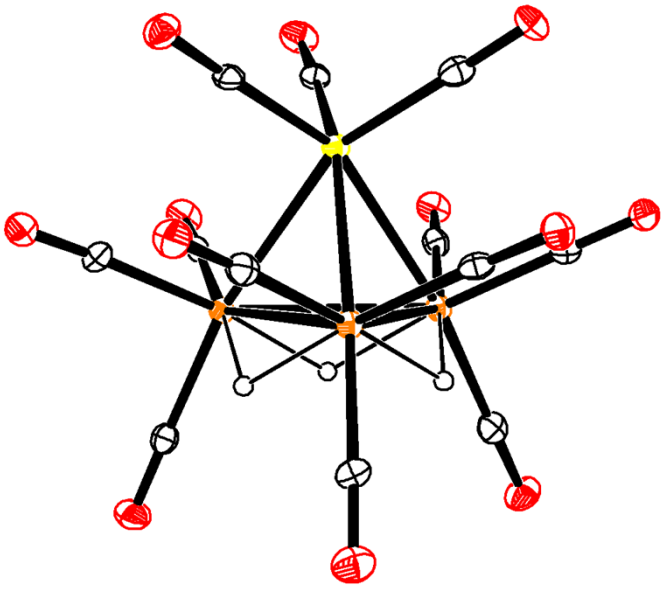

Figure S40. ORTEP drawing of $H_3Ru_3Ir(CO)_{12}$ (**3**) (orange Ru; yellow Ir; red O; grey C; white H). Thermal ellipsoids are at the 30% probability level.

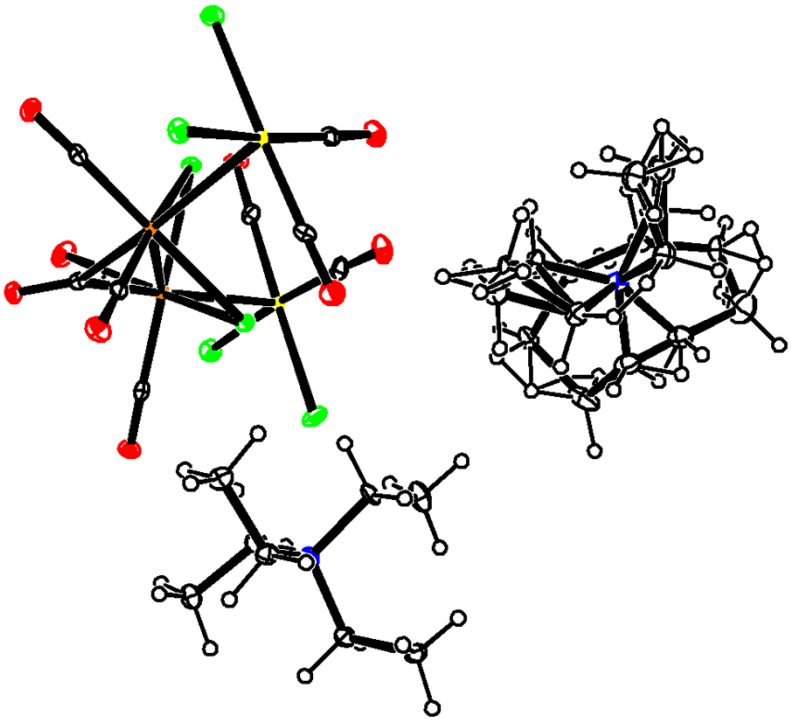

Figure S41. ORTEP drawing of $[NEt_4]_2[Ru_3Ir_2Cl_6(CO)_9]$ ($[NEt_4]_2$[**5**]) (orange Ru; yellow Ir; green Cl; red O; blue N; grey C; white H). Thermal ellipsoids are at the 30% probability level. Disordered atoms are included.

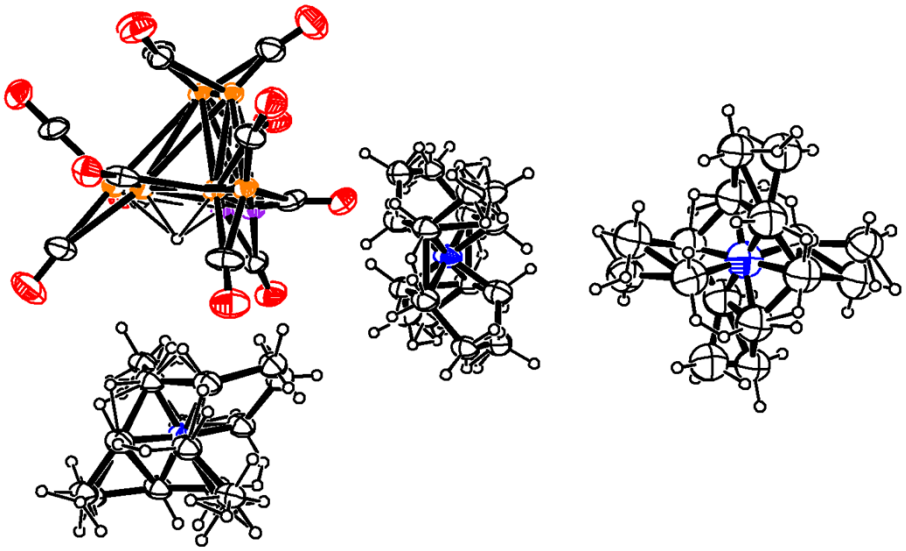

Figure S42. ORTEP drawing of $[NEt_4]_2[HRu_3Rh(CO)_{12}]$ ($[NEt_4]_2$[**6**]) (orange Ru; purple Rh; red O; blue N; grey C; white H). Thermal ellipsoids are at the 30% probability level. Disordered atoms are included.

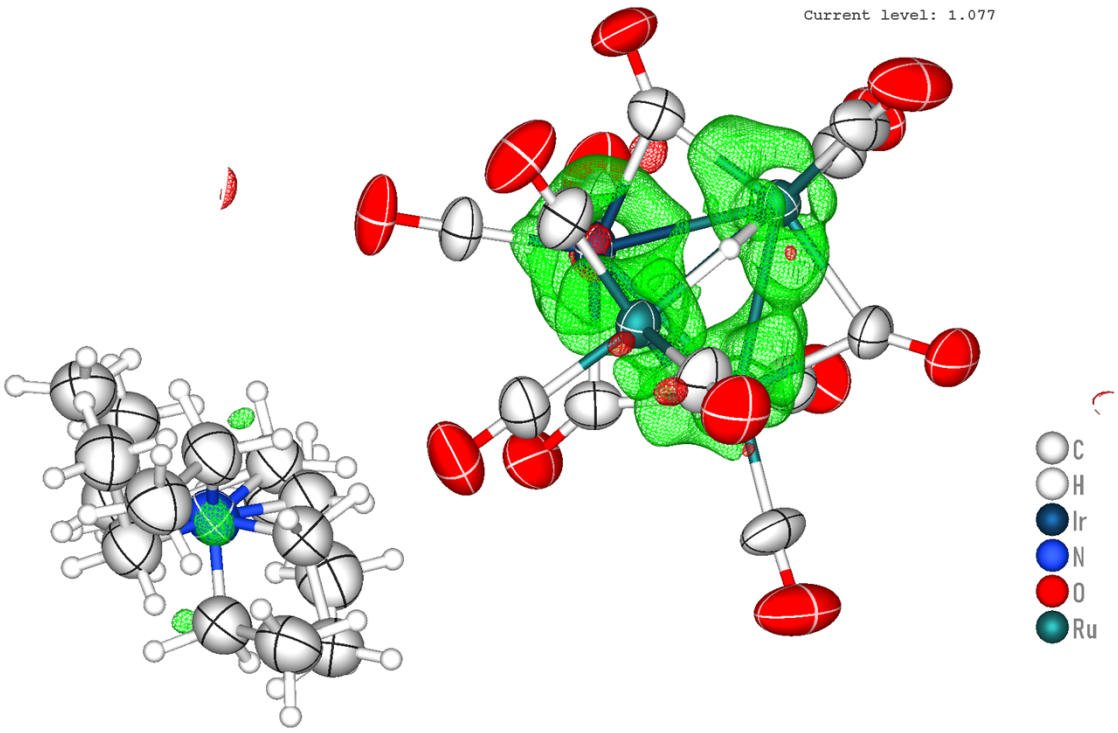

Figure S42. Residual electron density plot of $[NEt_4][H_2Ru_3Ir(CO)_{12}]$ ($[NEt_4][\mathbf{2}]$).

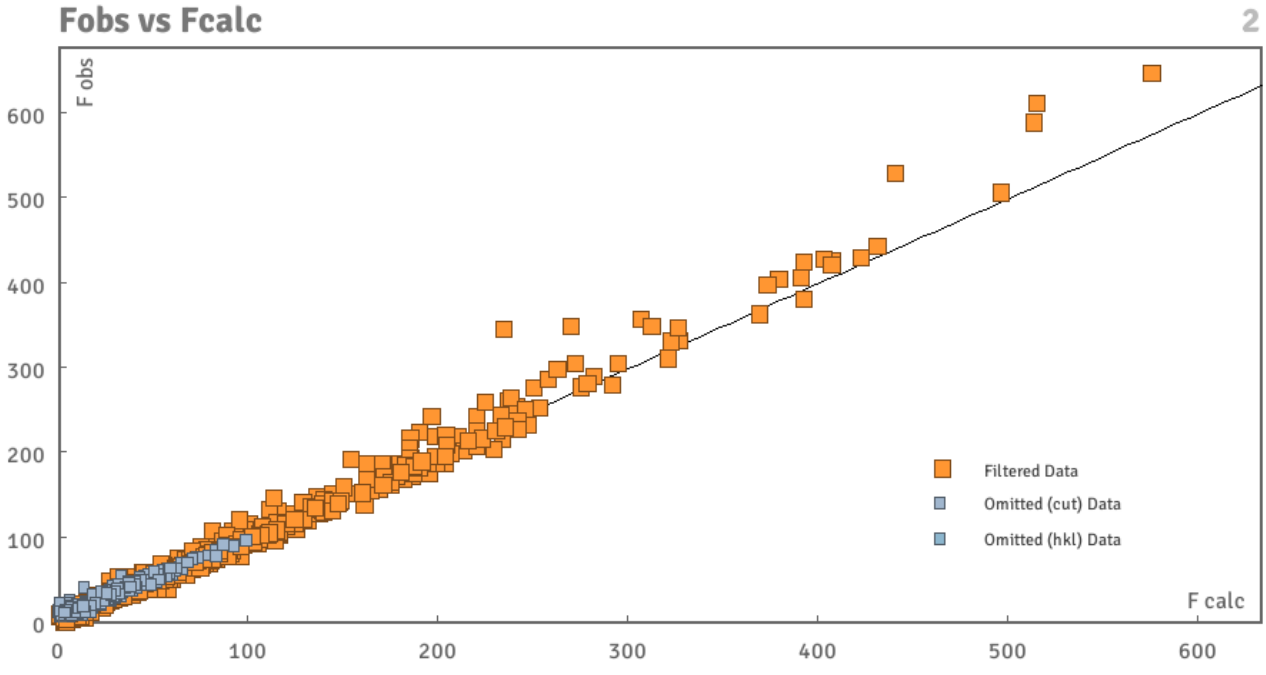

Figure S43. F_{obs} *vs*. F_{calc} plot of $[NEt_4][H_2Ru_3Ir(CO)_{12}]$ ($[NEt_4][\mathbf{2}]$).

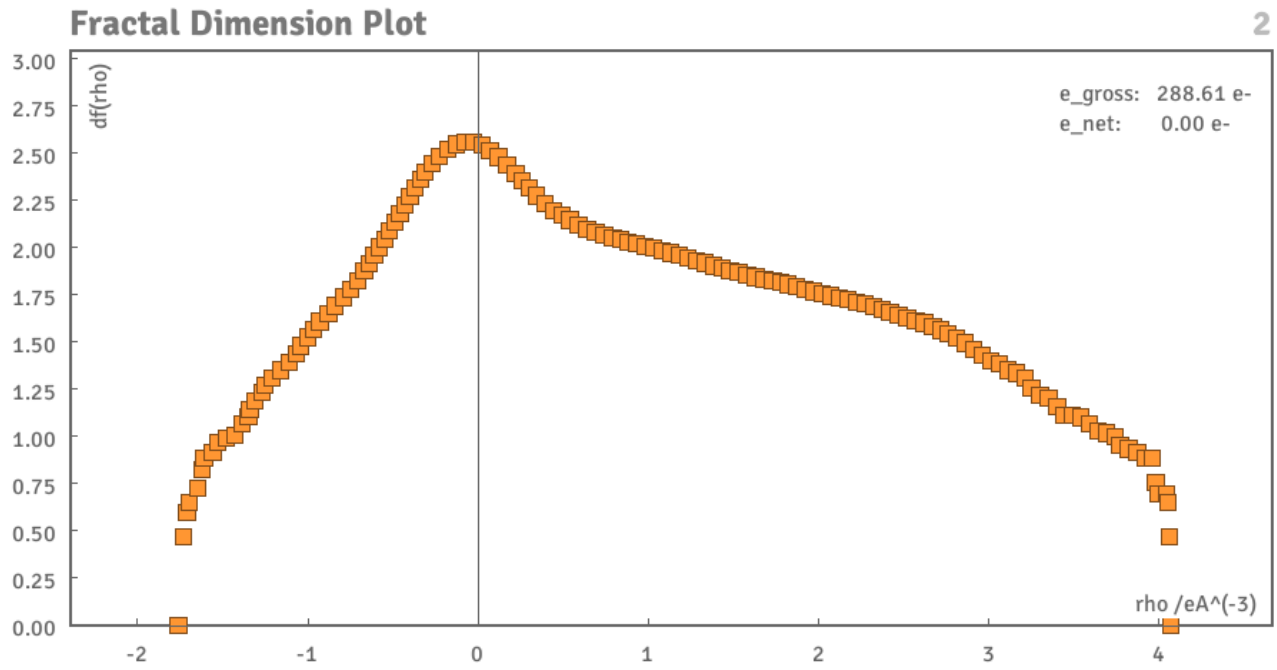

Figure S44. Fractal Dimension plot of $[NEt_4][H_2Ru_3Ir(CO)_{12}]$ ($[NEt_4][$**2**$]$).

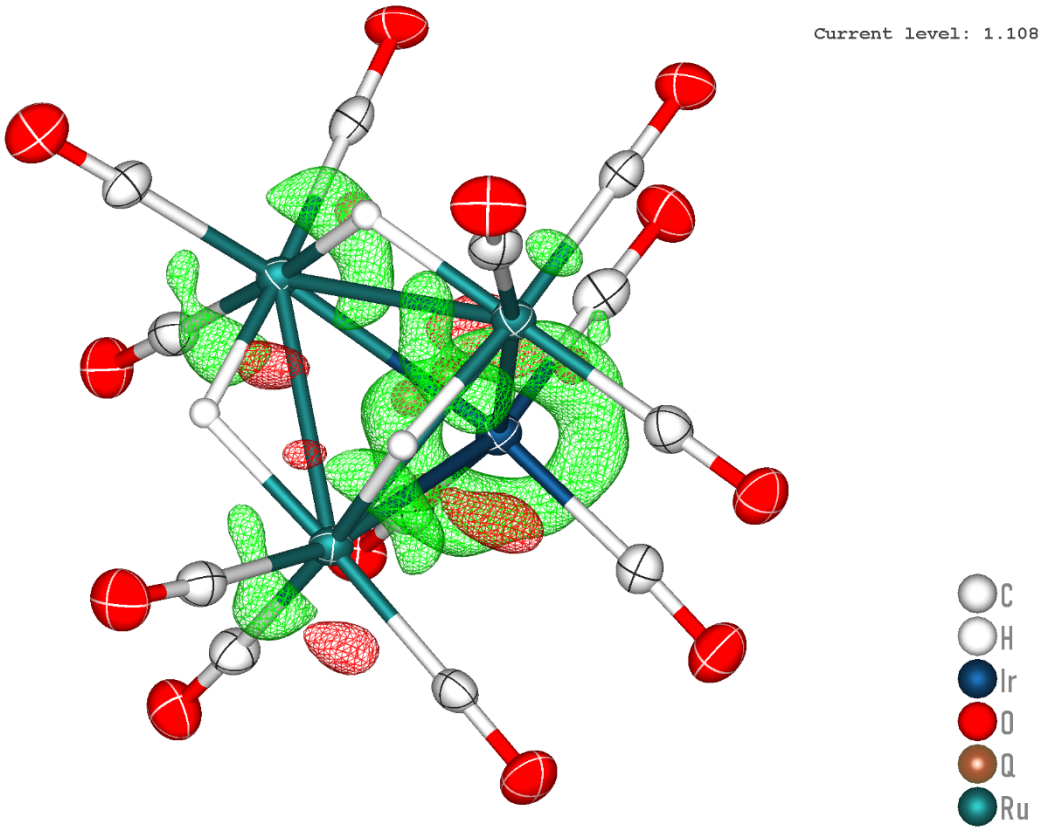

Figure S45. Residual electron density plot of $H_3Ru_3Ir(CO)_{12}$ (**3**).

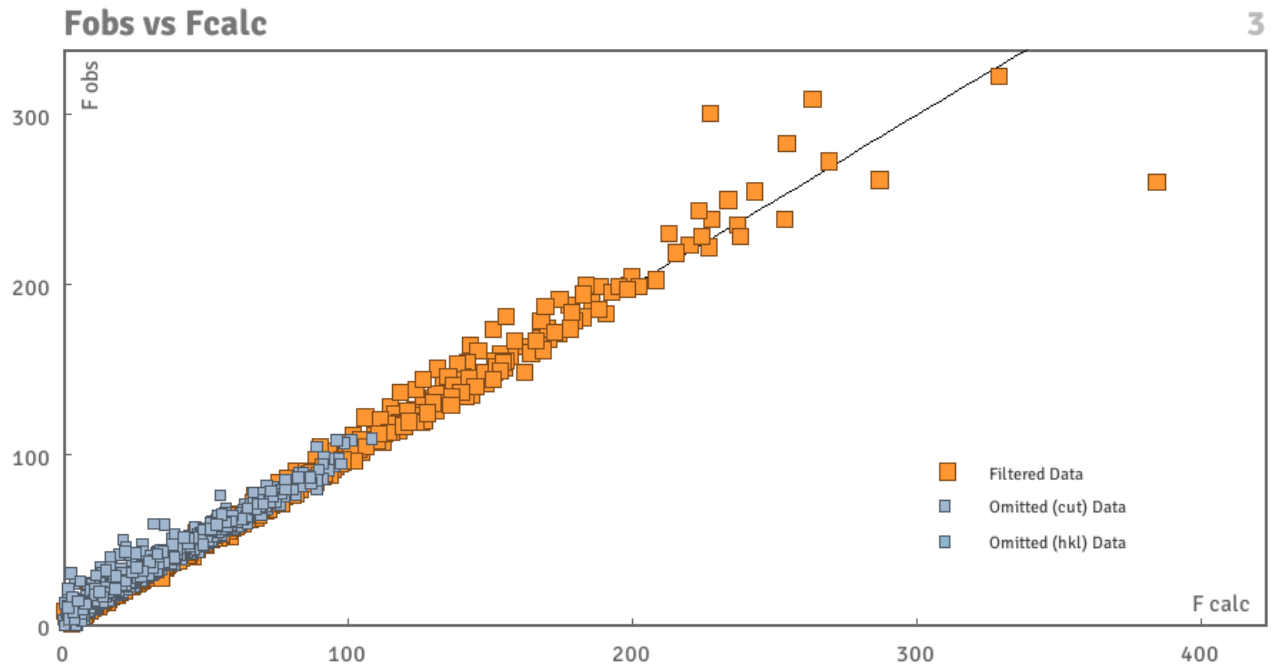

Figure S46. F_{obs} *vs*. F_{calc} plot of $H_3Ru_3Ir(CO)_{12}$ (**3**).

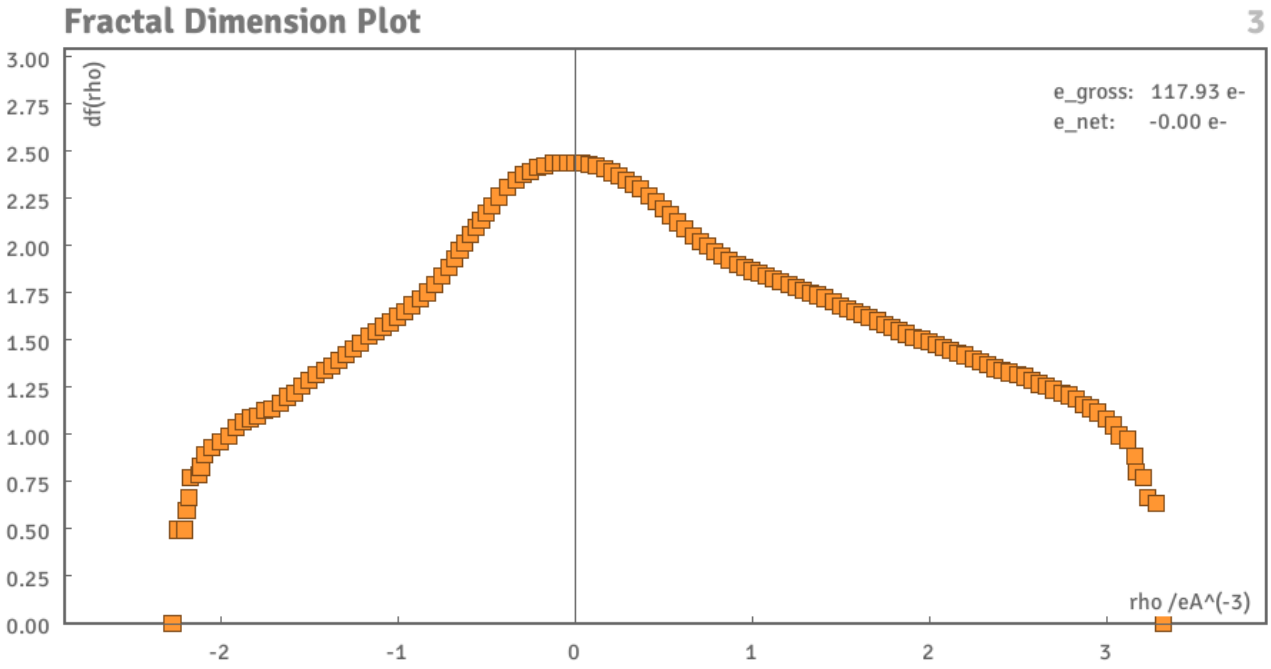

Figure S47. Fractal Dimension plot of $H_3Ru_3Ir(CO)_{12}$ (**3**).

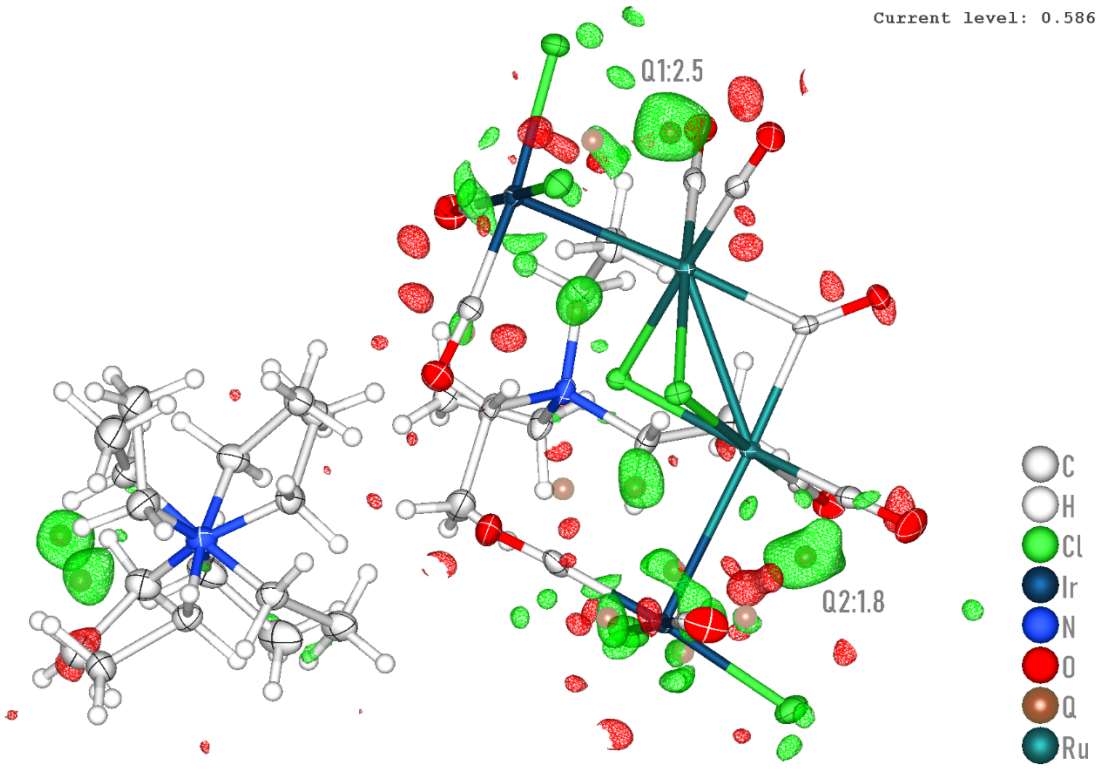

Figure S48. Residual electron density plot of $[NEt_4]_2[Ru_3Ir_2Cl_6(CO)_9]$ ($[NEt_4]_2$[**5**]).

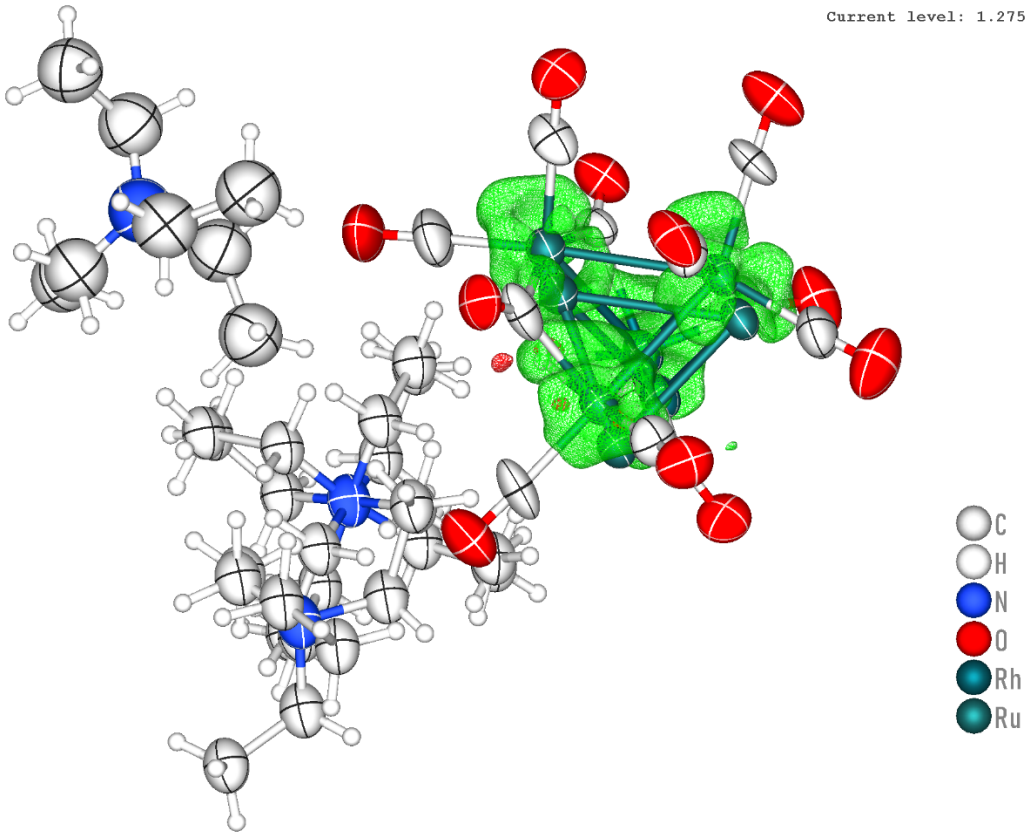

Figure S49. Residual electron density plot of $[NEt_4]_2[HRu_3Rh(CO)_{12}]$ ($[NEt_4]_2$[**6**]).

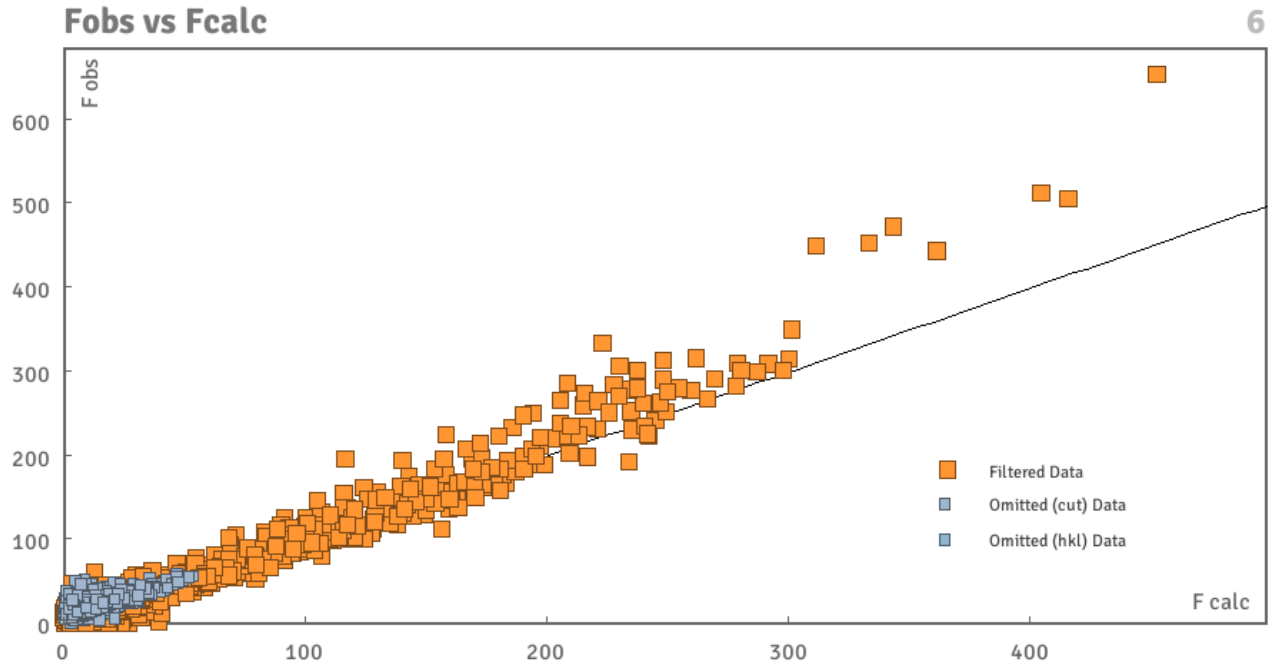

Figure S50. F_{obs} *vs*. F_{calc} plot of $[NEt_4]_2[HRu_3Rh(CO)_{12}]$ ($[NEt_4]_2$[**6**]).

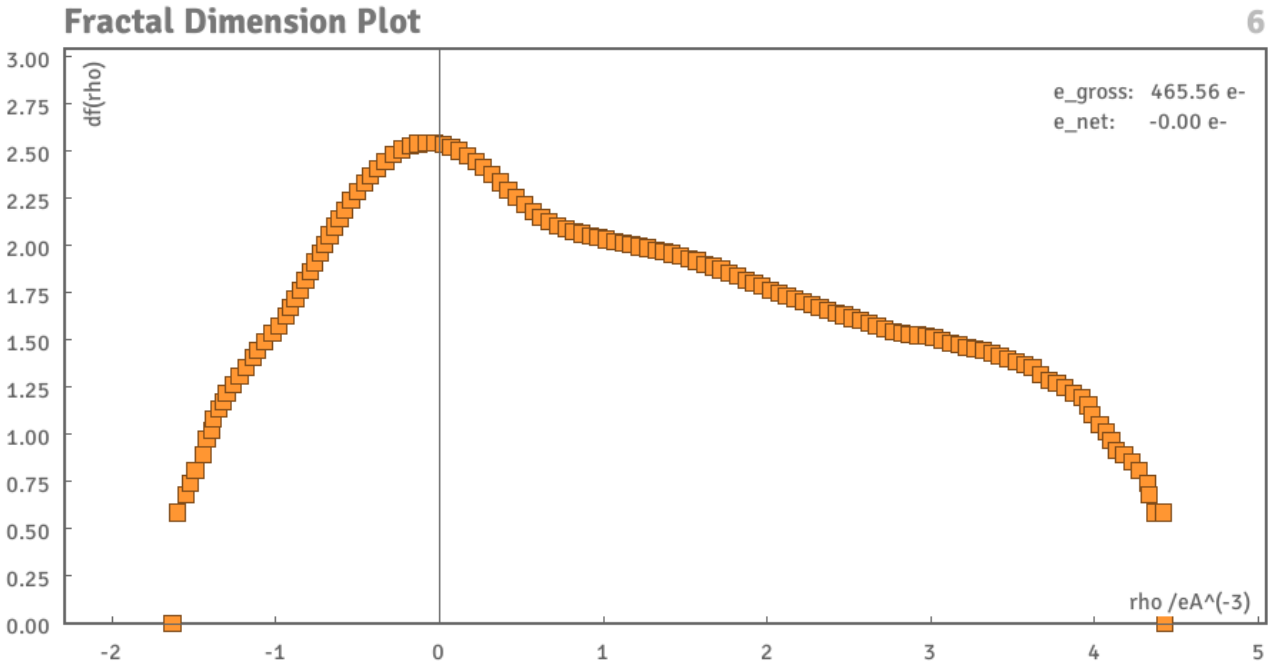

Figure S51. Fractal Dimension plot of $[NEt_4]_2[HRu_3Rh(CO)_{12}]$ ($[NEt_4]_2$[**6**]).